

## RESEARCH ARTICLE

10.1002/2017GC006813

## Key Points:

- Ridge segmentation is controlled by preexisting basement structures
- Spreading is perpendicular to the back-arc axis, allowing precise spreading directions to be determined
- Segment morphology reflects magma supply, which is locally enhanced by proximity to cross-arc volcanoes

## Supporting Information:

- Supporting Information S1

## Correspondence to:

M. O. Anderson,  
mande082@uottawa.ca

## Citation:

Anderson, M. O., W. W. Chadwick, Jr., M. D. Hannington, S. G. Merle, J. A. Resing, E. T. Baker, D. A. Butterfield, S. L. Walker, and N. Augustin (2017), Geological interpretation of volcanism and segmentation of the Mariana back-arc spreading center between 12.7°N and 18.3°N, *Geochem. Geophys. Geosyst.*, 18, 2240–2274, doi:10.1002/2017GC006813.


Received 11 JAN 2017

Accepted 26 MAR 2017

Accepted article online 23 MAY 2017

Published online 23 JUN 2017

## Geological interpretation of volcanism and segmentation of the Mariana back-arc spreading center between 12.7°N and 18.3°N

Melissa O. Anderson<sup>1,2</sup> , William W. Chadwick Jr.<sup>3</sup> , Mark D. Hannington<sup>1,2</sup>, Susan G. Merle<sup>3</sup> , Joseph A. Resing<sup>4</sup>, Edward T. Baker<sup>4</sup> , David A. Butterfield<sup>4</sup>, Sharon L. Walker<sup>5</sup>, and Nico Augustin<sup>2</sup> 

<sup>1</sup>Department of Earth Sciences, University of Ottawa, Ottawa, Ontario, Canada, <sup>2</sup>GEOMAR, Helmholtz Centre for Ocean Research Kiel, Kiel, Germany, <sup>3</sup>Cooperative Institute for Marine Resources Studies, Oregon State University and NOAA-PMEL, Hatfield Marine Science Center, Newport, Oregon, USA, <sup>4</sup>Joint Institute for the Study of Atmosphere and Ocean, University of Washington and NOAA-PMEL, Seattle, Washington, USA, <sup>5</sup>National Oceanic and Atmospheric Administration Pacific Marine Environmental Laboratory (NOAA-PMEL), Seattle, Washington, USA

**Abstract** The relationships between tectonic processes, magmatism, and hydrothermal venting along ~600 km of the slow-spreading Mariana back-arc between 12.7°N and 18.3°N reveal a number of similarities and differences compared to slow-spreading mid-ocean ridges. Analysis of the volcanic geomorphology and structure highlights the complexity of the back-arc spreading center. Here, ridge segmentation is controlled by large-scale basement structures that appear to predate back-arc rifting. These structures also control the orientation of the chains of cross-arc volcanoes that characterize this region. Segment-scale faulting is oriented perpendicular to the spreading direction, allowing precise spreading directions to be determined. Four morphologically distinct segment types are identified: dominantly magmatic segments (Type I); magmatic segments currently undergoing tectonic extension (Type II); dominantly tectonic segments (Type III); and tectonic segments currently undergoing magmatic extension (Type IV). Variations in axial morphology (including eruption styles, neovolcanic eruption volumes, and faulting) reflect magma supply, which is locally enhanced by cross-arc volcanism associated with N-S compression along the 16.5°N and 17.0°N segments. In contrast, cross-arc seismicity is associated with N-S extension and increased faulting along the 14.5°N segment, with structures that are interpreted to be oceanic core complexes—the first with high-resolution bathymetry described in an active back-arc basin. Hydrothermal venting associated with recent magmatism has been discovered along all segment types.

### 1. Introduction

The Mariana back-arc in the western Pacific is a slow-spreading center with highly complex tectonics with variable magmatic and hydrothermal activity (Figure 1). Processes of crustal accretion in the Mariana back-arc share some similarities with the Mid-Atlantic Ridge, both being characterized by strong ridge segmentation along large shear zone offsets and nontransform ridge-axis discontinuities. Individual segments on slow-spreading ridges may exhibit several important variations along strike: (1) increased magmatic activity toward the center of the segment, (2) increased crustal thickness toward the ends of the segment, and (3) increased fault size toward the ends of the segment [e.g., *Devey et al.*, 2010]. However, ridges associated with back-arc spreading have additional complexities resulting from oblique subduction, irregular trench geometries, strongly asymmetric spreading, subduction-zone collisions, slab reorientation, variations in spreading rates, and variable contributions of arc magmas [e.g., *Jenner et al.*, 1987; *Vallier et al.*, 1991; *Taylor*, 1995; *Stern*, 2002; *Kato et al.*, 2003; *Stern*, 2010; *Stern et al.*, 2013]. The structure of the Mariana back-arc is highly variable and reflects a number of these effects; for example, deep axial valleys with variable depths and cross-sectional morphologies north of 13.6°N versus axial volcanic ridges lacking valleys and resembling fast-spreading centers such as the East Pacific Rise south of 13.6°N [*Fryer*, 1995; *Martínez et al.*, 2000; *Deschamps and Fujiwara*, 2003; *Deschamps et al.*, 2004; *Asada et al.*, 2007].

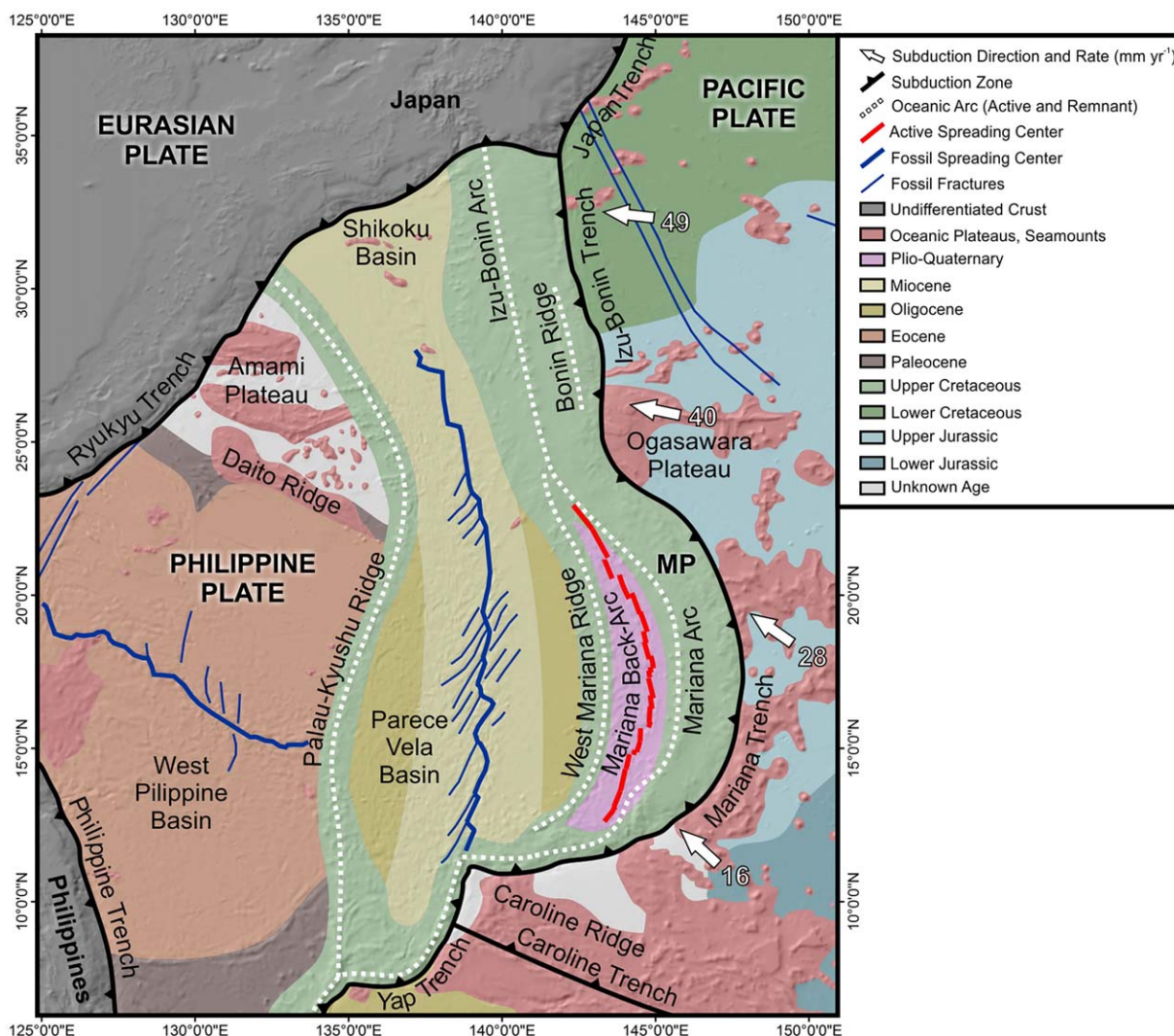


**Figure 1.** Tectonic setting of the Mariana subduction zone, overlain on regional bathymetry (GMRT v.3.2) [Ryan et al., 2009]. Ages of oceanic crust are from Bouysse et al. [2010] and references therein. Seafloor fractures are from Matthews et al. [2011] and Wessel et al. [2015]. Subduction rates are relative to the Philippine Plate, from deMets et al. [2010]. MP = Mariana Microplate.

Early investigations of the Mariana region were driven by the discovery of hydrothermal activity in the central back-arc during a series of *Alvin* dives in 1987, which located the Alice Springs (including Central Peak), Burke (including Snail Pits and Anemone Heaven), and Illium vent fields near 18°12'N, and the Central Trough vent field near 18°2'N [Craig et al., 1987; Campbell et al., 1987; Hessler et al., 1988; Hessler and Martin, 1989; Hessler and Lonsdale, 1991; Gamo and Shipboard Scientific Party, 1993; Fujikura et al., 1997; Ishibashi et al., 2015]. Venting was subsequently discovered in the southern back-arc near 13°N, beginning with the Forecast Seamount vent field in 1992 [Johnson et al., 1993; Gamo and Shipboard Scientific Party, 1993], the 13°N Ridge low-temperature vent field in 1999 [Mitsuzawa et al., 2000; Masuda et al., 2001], the Snail (also known as the “Fryer” site), Yamanaka (also known as the “Y” site), Pika, and Archean (3030–2980 mbsl) vent fields in 2003, and the Urashima vent field in 2010 [Wheat et al., 2003; Ishibashi et al., 2004; Urabe et al., 2004; Baker et al., 2005; Kakegawa et al., 2008; Yoshikawa et al., 2012; Nakamura et al., 2013; Ikehata et al., 2015]. However, the regional geological context of the different vent sites was poorly understood.

Here, we use nearly continuous high-resolution multibeam bathymetry collected by the *R/V Falkor* expedition FK151121 (20 November to 17 December 2015) over ~600 km of the Mariana back-arc spreading axis between ~13°N and ~18°N to assess the large-scale variations in axial morphology, and the relationships between tectonic processes, faulting, magma supply, and hydrothermal activity [Resing and Shipboard

*Scientific Party, 2016; Baker et al., 2016*]. The study area is divided into 11 segments, separated by first, second, and third-order discontinuities. We identify four morphologically distinct segment types, reflecting variable magma supply and structural evolution along the back-arc. We discuss the relationships between these features and the influence on hydrothermal venting. We also investigate the regional controls on ridge segmentation, and the effect of cross-arc structures on segment morphologies. Finally, segment-scale fault orientations are measured to reveal precise spreading directions along the Mariana back-arc.

## 2. Tectonic Setting

The ~2800 km long Izu-Bonin-Mariana (IBM) trench is characterized by the oblique subduction of some of the oldest oceanic lithosphere in the world, ranging in age from Early Cretaceous in the north and to Mid-Jurassic along the Mariana trench (Figure 1) [Jarrard, 1986; Müller *et al.*, 1997; Stern *et al.*, 2003]. The relative motions of the Pacific plate and the Philippine Sea plate result in a southward decrease in convergence rates along the IBM [deMets *et al.*, 1994]. Near the southern end of the Philippine Sea plate (8°N 137°18'E) [deMets *et al.*, 1994], the Pacific plate is moving NW relative to the Mariana trench at a rate of 16–28 mm yr<sup>-1</sup>, while along the Izu Bonin trench the Pacific plate is moving WNW at a rate of 40–49 mm yr<sup>-1</sup> (Figure 1) [deMets *et al.*, 2010]. Several phases of clockwise rotation of the Philippine Sea plate, beginning in the Eocene, affected the region [Uyeda and Ben-Avraham, 1972; Koyama *et al.*, 1992; Hall *et al.*, 1995; Sdrolias *et al.*, 2004], first with the northward migration of the Izu-Bonin trench and opening of the West Philippine back-arc basin between 55 and 33–30 Ma (Figure 1) [Hilde and Lee, 1984; Deschamps and Lallemand, 2002]. By 30–15 Ma, the Izu-Bonin trench had migrated almost ~1000 km to the north, accompanied by the opening of the Shikoku basin, while the Mariana trench migrated ~400 km to the north, accompanied by the opening of the Parece Vela basin (Figure 1) [Seno and Maruyama, 1984; Seno, 1985; Okino *et al.*, 1998; Sdrolias *et al.*, 2004]. At ~25 Ma, the arrival of much older oceanic lithosphere (110–130 Ma crust from the Pacific plate) caused southward steepening of the IBM slab that is thought to have increased back-arc spreading and trench migration [Seno, 1985; le Pichon and Huchon, 1987; Carlson and Mortera-Gutiérrez, 1990]. In the late Miocene-Pliocene, subduction initiated farther south along the Philippine trench, and clockwise rotation of the Philippine Sea plate resumed, retreating from the Mariana trench faster than from the Izu-Bonin trench [Seno, 1985]. This resulted in renewed spreading in the Mariana back-arc at ~7 Ma, with true seafloor spreading initiating at 3–4 Ma, forming the Mariana Microplate (Figures 1 and 2) [Scott *et al.*, 1981; Masuda *et al.*, 1994; Martínez *et al.*, 1995; Stern *et al.*, 2003]. Spreading continues today in the Mariana back-arc basin, with an opening rate of ~15 to 45 mm yr<sup>-1</sup>, increasing southward [Kato *et al.*, 2003; Stern *et al.*, 2003].

Differences in the rate of trench migration in the Izu-Bonin and Mariana subduction zones correspond to different slab dips and morphologies [van der Hilst and Seno, 1993; Miller *et al.*, 2004]. Seismic tomography indicates that the Izu-Bonin slab deflects horizontally at the 670 km discontinuity in the upper mantle, whereas the Mariana slab dips almost vertically into the lower mantle [van der Hilst and Seno, 1993; Engdahl *et al.*, 1998; Widiyantoro *et al.*, 1999]. The dramatic change in slab trajectory is accommodated by tearing at the junction of the Izu-Bonin and Mariana arcs [Miller *et al.*, 2004]. A possible slab tear also has been suggested at the southern end of the Mariana arc, where there is a sharp curve in the Challenger Deep segment [Fryer *et al.*, 2003; Gvirtzman and Stern, 2004; Miller *et al.*, 2006].

Several different mechanisms have been proposed to explain the modern crescent shape of the Mariana trench (Figures 1 and 2). Karig [1971a, 1971b] suggested that the shape of the back-arc and variations in spreading rate are related to the nonrigid behavior of the arc and fore arc. Bracey and Ogden [1972] suggested that the basin formed as a result of rifting of the arc first at the center and then progressing northward and southward, contributing to the crescent shape of the arc. Le Pichon *et al.* [1985] proposed a rigid plate model with a single pole of rotation at ~21°N/138°E, although several studies demonstrated that a single pole cannot account for the basin geometry [Karig *et al.*, 1978; Fryer and Hussong, 1981; Stern *et al.*, 1984]. Most authors agree that collisions of buoyant oceanic plateaus with the IBM subduction zone effectively “pinned” the top and bottom of the Mariana trench, while continued eastward rollback at the center produced the curved shape [Vogt, 1973; Vogt *et al.*, 1976; McCabe and Uyeda, 1983; Hsui and Youngquist, 1985; Carlson and Mortera-Gutiérrez, 1990; Taylor, 1992; Scholz and Small, 1997; Miller *et al.*, 2004; Miller *et al.*, 2005; Wallace *et al.*, 2005; Miller *et al.*, 2006]. In the south at ~10°N, the Mariana trench abuts the Caroline Ridge (Figure 1). In the north at ~26°N, the Ogasawara Plateau (also known as the Marcus-Necker Ridge,



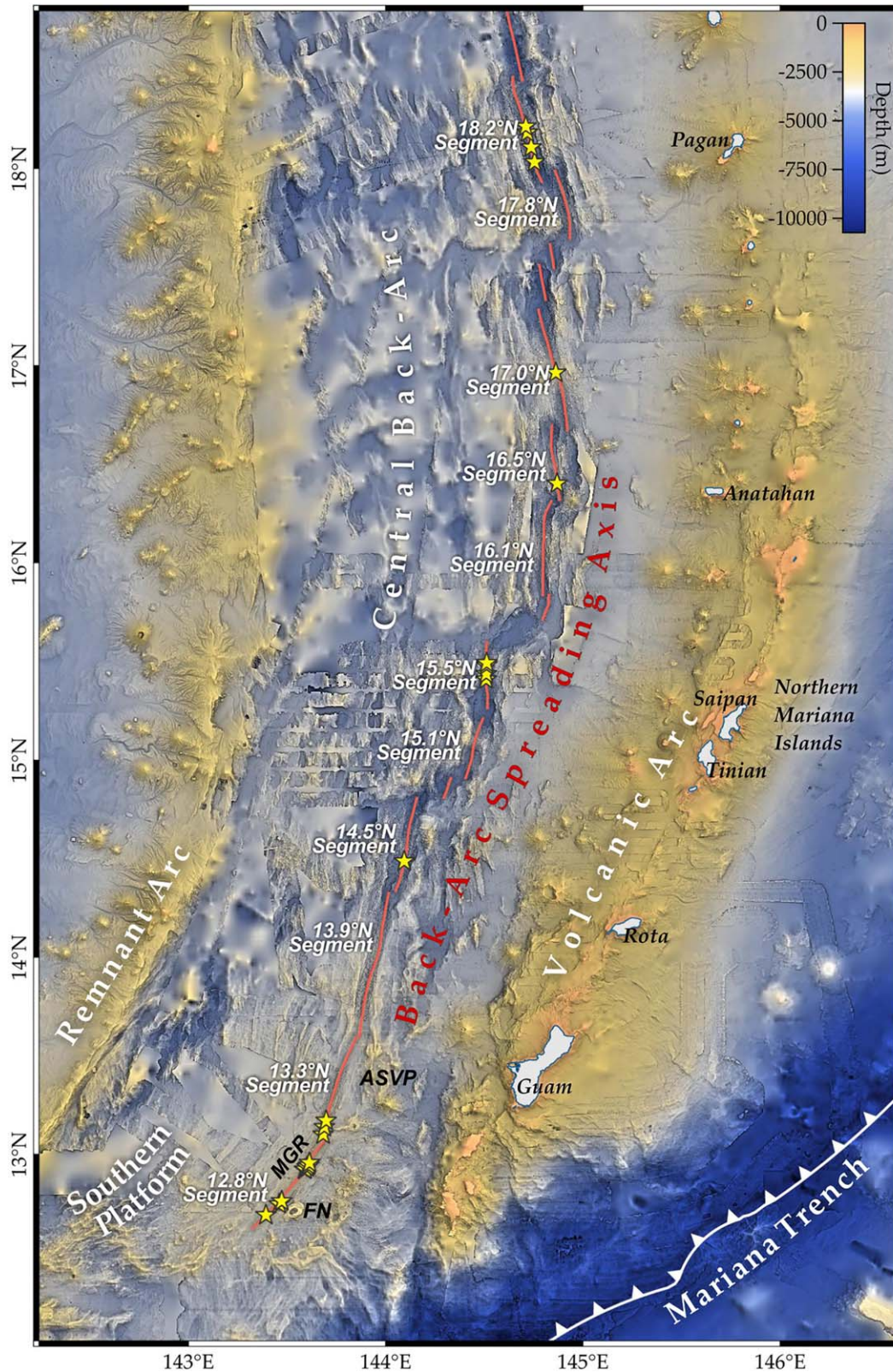


**Figure 2.** Bathymetry of the Mariana back-arc with the segment nomenclature, with data from the Global Multi-Resolution Topography Synthesis (GMRT v3.2) [Ryan *et al.*, 2009], the FK151121 expedition aboard the *R/V Falkor* in 2015 [Resing and Shipboard Scientific Party, 2016], and the EX1605L1–2 expeditions aboard the *R/V Okeanos Explorer* in 2016 [Gray, 2016; Lobecker, 2016]. Yellow stars indicate hydrothermal vent sites discovered along the back-arc from Resing and Shipboard Scientific Party [2016] and Baker *et al.* [2016]. ASVP = Alphabet Seamount Volcanic Province; FN = Fina Nagu volcanic complex; MGR = Malaguana-Gadao Ridge.

Michelson Ridge, or Mid-Pacific Mountains) occurs at the junction between the Izu-Bonin and Mariana trenches (Figure 1). Trench modification by collision of oceanic plateaus is supported by the three-dimensional numerical modeling of *Mason et al.* [2010], and is currently the most widely accepted explanation for the highly arcuate shape of the Mariana trench.

*DeMets et al.* [2010] showed that extension in the back-arc is associated with the eastward displacement of the Mariana trench at  $\sim 20 \text{ mm yr}^{-1}$  relative to the Philippine plate. The southern segments of the Mariana back-arc have full-spreading rates of  $45 \text{ mm yr}^{-1}$  [*Kato et al.*, 2003]. The central segments have slow spreading rates of  $25\text{--}40 \text{ mm yr}^{-1}$  [*Kato et al.*, 2003], and the spreading is 2–3 times faster to the west than to the east [*Deschamps and Fujiwara*, 2003]. In the central Mariana back-arc near  $18^\circ\text{N}$ , *Fryer* [1981] noted a major difference in seafloor morphology between the western and eastern sides of the basin. The western side is characterized by extensively block-faulted terrain over 60 km in width, whereas the eastern side contains evenly spaced ridges and troughs that resemble abyssal hill morphologies adjacent to the active spreading axis (Figure 2). *Fryer* [1981] suggested that this morphology resulted from a two-stage evolution of the back-arc basin, with initial stretching and collapse of the arc during the first few million years of extension producing the block-faulted terrain, followed by a transition to true seafloor spreading producing the ridge-transform morphology. Major fracture zones (deep valleys that extend across the back-arc region) were originally identified by *Kong* [1993], and *Hawkins et al.* [1990] described numerous minor discontinuities in the back-arc spreading axis. Near the back-arc spreading center, these fracture zones are associated with major ridge offsets that display a strong sinistral shear component (referred to here as shear zone offsets, or SZOs), and are highly oblique to the spreading axis, unlike transform fractures at mid-ocean ridges. The morphology of the seafloor also varies considerably between the northern, central, and southern parts of the back-arc (Figure 2) [*Fryer and Hussong*, 1981; *Hussong and Uyeda*, 1981; *Macdonald*, 1982; *Sinton and Hussong*, 1983; *Kong et al.*, 1992; *Seama and Fujiwara*, 1993; *Fryer*, 1995; *Baker et al.*, 1996; *Stüben et al.*, 1998; *Martínez et al.*, 2000; *Deschamps and Fujiwara*, 2003; *Deschamps et al.*, 2004; *Asada et al.*, 2007]. The slow-spreading morphology of the central segment is thought to correspond to a greater crustal thickness in this region of 4–7 km [*Ambos and Hussong*, 1982; *Bibee et al.*, 1980; *LaTraille and Hussong*, 1980; *Sinton and Hussong*, 1983]. In the north ( $21^\circ\text{N}$  to  $22^\circ\text{N}$  latitude), the full-spreading rate is even slower, at  $\sim 10\text{--}15 \text{ mm yr}^{-1}$  [*Yamazaki et al.*, 1993]. Progressive changes in isotopic and geochemical compositions of basaltic glasses along the length of the Mariana back-arc were reported by *Gribble et al.* [1996] and *Gribble et al.* [1998], who identified a mature arc component with increased partial melting in the northernmost rift compared to the “true” back-arc basin basalts of the central back-arc. The proportion of the subduction component also decreases southward in the central back-arc [*Gribble et al.*, 1996].

A notable feature of the Mariana back-arc is the occurrence of cross-arc chains of volcanoes that extend westward from the presently active volcanic arc and are also present on the remnant arc [*Fryer and Hussong*, 1982; *Dixon and Stern*, 1983; *Fryer*, 1995; *Heeszel et al.*, 2008; *Stern et al.*, 2014]. Several of these “cross-arc chains” are seismically active [*Heeszel et al.*, 2008]. Near the active volcanic arc, these structures are undergoing  $\sim\text{N-S}$  extension [*Heeszel et al.*, 2008], consistent with GPS measurements of the islands, which are moving apart in a N-S direction [*Kato et al.*, 2003]. The regime where the cross-arc chains are located shifts from extension at the volcanic front to compression further to the west, reflecting the stresses associated with the bend in the arc [*Heeszel et al.*, 2008]. *Fryer and Hussong* [1982] suggested the volcanism associated with the cross-arc chains results from a complex interaction of preexisting structures, fore-arc tectonics, arc magmatism, and back-arc rifting. Here, we examine these structures and their role in back-arc segmentation, segment morphology, and magmatism in the southern and central back-arc.

### 3. Methods

Ship-based multibeam bathymetric data from the active Mariana back-arc was collected during the R/V *Falkor* expedition FK151121 [*Resing and Shipboard Scientific Party*, 2016] and the R/V *Okeanos Explorer* expedition EX1605L1–2 [*Gray*, 2016; *Lobecker*, 2016], as shown in Figure 2. The *Falkor* and the *Okeanos Explorer* were both equipped with Kongsberg Maritime EM 302 multibeam echo sounders with operating frequencies of 30 kHz, capable of mapping seawater depths of up to 7000 m. The data were gridded with a cell size of 40 m. To create geological maps of the active back-arc spreading center, the bathymetric data were



interpreted with the aid of acoustic backscatter, slope shading, and rugosity and were further processed using the “Terrain Texture Shading” (TTS) technique (supporting information Figure S1) developed by Brown [2010]. Terrain Texture Shading combines traditional hill shading with curvature analysis to add texture to shaded relief [e.g., Kennelly, 2008; Kennelly and Stewart, 2014; Augustin et al., 2016]. This technique can increase the contrast of geological and structural features, and has recently been applied to bathymetric data in different tectonic settings [e.g., Anderson et al., 2016; Augustin et al., 2016].

We identified 11 separate segments along the Mariana back-arc spreading center that are between 33 and ~82 km long and ~6–25 km wide (Figure 2). The mapped segments are between 12°52'N and 18°36'N and cover an area of ~23,250 km<sup>2</sup>. Individual segments are separated by first and second-order discontinuities, including three major shear zone offsets and numerous minor discontinuities. These include overlapping spreading centers (OSCs) and deviations in axial linearity (DEVALS) defined by sharp changes in spreading axis orientation with very little offset. Both OSCs and DEVALS are characterized by zones of discordant topography and highly variable structural orientations. Compared to previous work on the segmentation of the Mariana back-arc spreading center by Stüben et al. [1998], this study provides higher-resolution bathymetry, improved geographical precision, and a more precise identification of the spreading axis, leading to a better understanding of the relationships between geological units and the nature of the ridge offsets. The eight ridge segments identified by Stüben et al. [1998] broadly correlate with the segments identified here (Figure 2): segment 1 [Stüben et al., 1998] = the 17.0°N segment [this study]; segments 2, 3, and 4 [Stüben et al., 1998] are likely misidentified and occur to the west of the 16.5°N segment [this study]; segment 5 [Stüben et al., 1998] = the 16.1°N segment [this study]; segment 6 [Stüben et al., 1998] = the 15.5°N segment [this study]; segment 7 [Stüben et al., 1998] = the 15.1°N segment [this study]; and segment 8 [Stüben et al., 1998] = the 14.5°N segment [this study].

Different styles of faulting in this study were identified in the gridded bathymetry from scarps associated with high-intensity linear backscatter reflectors when facing inwards and low-backscatter shadows when facing outward. The faults were mapped with the fault scarp direction indicated, and the vertical offsets were estimated using the depth differences between two points on either side of the scarp at the center of the fault in map view. The geometry and spatial arrangement of faults, including azimuth distribution, were compiled and analyzed to distinguish areas of pure extension from those with a strike-slip component.

The map legend used in subsequent figures (also shown in supporting information Figure S2) follows Anderson et al. [2016] and is based on established classifications of volcanic geomorphology and seafloor structure [cf., Walker, 1993; Thouret, 1999; Sigurdsson, 2000]. Interpretation of map units was based on ground-truth data from earlier observations made during submersible dives with *Alvin* at ~18°N in 1987 [Craig et al., 1987; Campbell et al., 1987; Hessler et al., 1988; Gamo and Shipboard Scientific Party, 1993], with *Shinkai 6500* near ~13°N in 1992 (Y9204 TRANSARC expedition) [Johnson et al., 1993; Gamo and Shipboard Scientific Party, 1993] and at ~17°N in 2008 (JAMSTEC expedition YK08–08 Leg-1) [Fujiwara et al., 2008], from seafloor images captured by the towed ocean floor observation system and TV-grab between 14°45'N and 17°40'N during the *Sonne* SO-69 cruise in 1990 [Stüben et al., 1998], from near-bottom photo surveys at 15.5°N and 17°N by AUV *Sentry* in 2015 (expedition FK151121) [Resing and Shipboard Scientific Party, 2016], ROV *Deep Discoverer* dives at 15.5°N and 17°N in 2016 (expedition EX1605L1) [Gray, 2016], and ROV *SuBastian* dives at 15.5°N, 17°N, and 18°N in 2016 (expedition FK161129) [Butterfield et al., 2017] (Figure 3). Comparisons with ground-truthed acoustic backscatter in other similar studies [e.g., Yeo et al., 2012, 2016; Anderson et al., 2016] provide additional confidence in our interpretations. Relative ages of the geological units were interpreted from overlapping relationships and sediment cover from backscatter intensity [cf., Hewitt et al., 2010]. All contacts are inferred. Hydrothermal vent sites (yellow stars, Figure 2) along the back-arc were identified during plume surveys of the FK151121 cruise [Resing and Shipboard Scientific Party, 2016; Baker et al., 2016], with seafloor observations confirming active venting during the EX1605L-1 cruise [Gray, 2016] and the FK161129 cruise [Butterfield et al., 2017].

Quantitative map data are reported in terms of the parameters shown in Figure 4 and summarized in Table 1: (1) segment length, measured along the back-arc spreading axis; (2) segment width,  $W$ , measured perpendicularly between the tops of the axial valley walls; (3) axial valley relief,  $d$ , measured from the deepest part of the axial valley to the highest point of the axial wall; (4) skewness,  $s$ , as the difference in height across an axial valley; and (5) axial volcanic ridge height,  $r$ , measured from the deepest part of the axial valley to the top of the

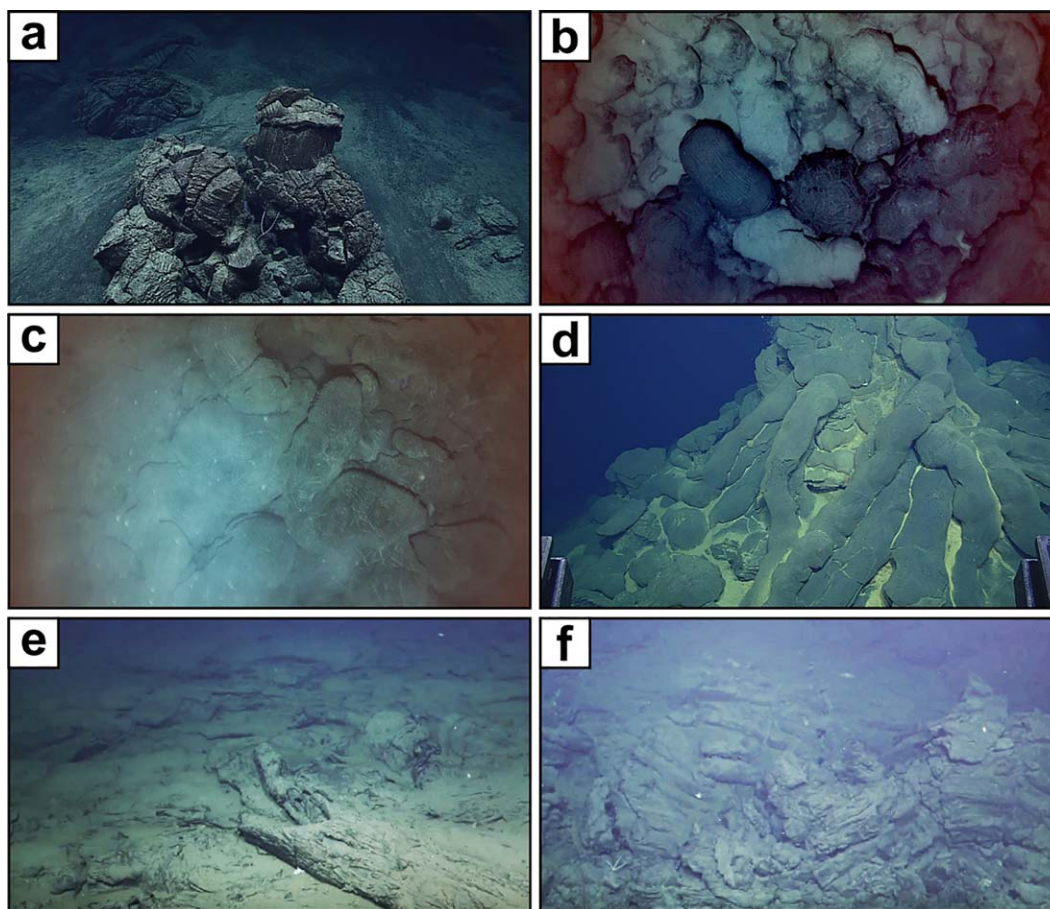


**Figure 3.** Seafloor observations of lava morphologies and hydrothermal venting along the Mariana back-arc: (a) small isolated pillow lava outcrop surrounded by thick sediment (EX1605L-1 cruise; ROV dive 9) [Gray, 2016]; (b) older sedimented pillow flows overlain by young pillow flows (FK151121 cruise; AUV *Sentry* dive 367) [Resing and Shipboard Scientific Party, 2016]; (c) diffuse low-temperature diffuse venting emanating from a young pillow flow (FK151121 cruise; AUV *Sentry* dive 367) [Resing et al., 2016]; (d) large pillow mound with low-temperature iron-stained hydrothermal precipitates (EX1605L-1 cruise; ROV dive 9) [Gray, 2016]; (e) sedimented ropey sheet flows that characterize the “smooth volcanic terrain” of the 17.0°N segment (FK161129 cruise; ROV dive S41) [Butterfield et al., 2017]; and (f) jumbled sheet flows along the 17.0°N segment (FK161129 cruise; ROV dive S41) [Butterfield et al., 2017].

central volcanic ridge. These measurements were made along 31 profiles across the mapped segments of the back-arc, perpendicular to spreading direction. Cross-sectional profiles were generated in ArcGIS® v.10.1 and were drafted to include the mapped geological features.

#### 4. Mapped Features

Despite variations in gross segment morphologies, we identify the fundamental geological units that occur throughout the southern and central back-arc. These units are classified as “old BAB crust,” “neovolcanic terrain,” “volcanoes,” “deep sedimented basins,” and “structures,” as described below, which form the basis of the legend in Figures 5–14. We present a series of geological maps along each segment to show the distribution of these features (section 5; Figures 5–14), in order to provide insight into the evolution of the back-arc and the relationship between tectonics and volcanism along the spreading center.

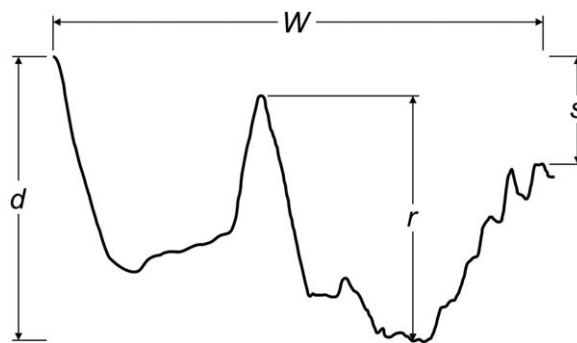


**Figure 4.** Example of a cross-axis bathymetric profile with morphological parameters used in Table 1 and described in text:  $W$  = segment width,  $d$  = axial valley depth,  $r$  = axial volcanic ridge height,  $s$  = skewness.

**Table 1.** Morphologies and Important Features of the Back-Arc segments

	Segment Length (km)	Distance to Arc (km)	Full Spreading Rate (mm yr <sup>-1</sup> ) <sup>a</sup>	Neo-Volcanic Volume (km <sup>3</sup> ) <sup>b</sup>	Segment Width W (km) <sup>c</sup>	Eruption Rate per km (m <sup>3</sup> yr <sup>-1</sup> km <sup>-1</sup> ) <sup>b</sup>	Maximum Seafloor Depth (mbsl)	Axial Valley Relief d (m) <sup>c</sup>	Skewness s (m) <sup>c</sup>	Axial Volcanic Ridge Relief r (m) <sup>c</sup>	Segment Type <sup>d</sup>	Hydro-thermal Venting?
Southern Back-Arc												
12.8°N Segment A-A'	65	25			17		3400	N/A	0	500	I	Y
13.3°N Segment B-B'	59	25	45		14		3450	400	200	550	I	Y
C-C'					18		3700	400	50	550		
Central Back-Arc												
13.9°N Segment D-D'	82	68	~42.5	145		9377					III	N
E-E'					11		3350	550	0	200		
F-F'					8		3600	250	50	100		
14.5°N Segment G-G'	49	86	~41.5	271		9979					III	Y
H-H'					12		4350	600	50	300		
I-I'					23		4500	1100	200	800		
15.1°N Segment J-J'	33	84	40	118		6219					III	N
K-K'					13		4550	1300	700	200		
L-L'					25		4550	1200	600	650		
15.5°N Segment M-M'	34	101	~38	84		3912					IV	Y
N-N'					22		4650	1300	500	300		
O-O'					24		4400	1300	100	1050		
16.1°N Segment P-P'	64	95	35	163		11143					III	N
Q-Q'					25		4300	1200	150	350		
R-R'					8		4200	850	300	150		
16.5°N Segment S-S'	42	97	~32	108		10,286					II	Y
T-T'					10		4050	650	400	350		
U-U'					8		3950	500	250	N/A		
17.0°N Segment V-V'	70	103	28	474		31,600					II	Y
W-W'					13.5		4500	1100	300	500		
X-X'					18		4150	600	100	200		
Y-Y'					6		3300	450	100	0		
17.8°N Segment Z-Z'	39	97	~26	83		3458					III	N
AA-AA'					11		3350	500	50	150		
BB-BB'					19		4550	1500	1400	200		
18.2°N Segment CC-CC'	61	113	25	401		11,739					IV	Y
DD-DD'					15		4300	1000	200	250		
EE-EE'					16		4250	1250	550	350		
					10		4650	1300	200	500		
					16		4750	1350	150	950		
					14		3900	600	0	250		
					16		4400	1300	650	800		

<sup>a</sup>Full spreading rates determined by GPS for some latitudes (Kato et al., 2003); extrapolated for intervening segments (indicated by ~).

<sup>b</sup>See supporting information and Table S2 for neovolcanic volume and eruption rate calculations.

<sup>c</sup>See Figure 4 for definitions of parameters.

<sup>d</sup>See text for segment type classification (summarized in Figure 17).

#### 4.1. Old BAB Crust

The axial valley walls of the central Mariana trough expose old back-arc basin (BAB) crust associated with back-arc spreading that is now at the flanks of the active spreading center. This unit is stratigraphically older than the neovolcanic products that occupy the axial valley floor. The features of the old BAB crust are classified here based on the surface morphology and backscatter intensity. “Hummocky old crust” is characterized by a rough surface (high rugosity), with a low to moderate slope, numerous small volcanic edifices, and minor faulting. The backscatter is uneven with a low to moderate intensity. “Faulted old crust” has a lower surface roughness but numerous normal faults with steep slopes identified as bright, curvilinear reflectors in otherwise low-intensity backscatter. “Sedimented old crust” is characterized by smooth surfaces with low relief, few normal faults, shallow slopes, and low and even backscatter intensity. The contacts between these different types of old crust are gradational. Dome-shaped bathymetric features with clear corrugated



surfaces at the sides of the axial valley are interpreted here to be “oceanic core complexes,” similar to those now commonly found on the slow-spreading Mid-Atlantic Ridge (MAR) [e.g., Tucholke *et al.*, 1998; MacLeod *et al.*, 2009]. While no sampling has been performed to confirm the presence of upper mantle rocks, these distinct bathymetric features are associated with mappable large-offset low-angle faults along the axial valley walls, and the corrugations on their upper surfaces extend ~6–7 km parallel to the direction of spreading. Near the tops of the core complexes, the seafloor morphology becomes more rugged with complex faulting patterns, which is consistent with observations of core complexes along the MAR, where sampling indicates that these elevated massifs are exposed magmatic crust [e.g., MacLeod *et al.*, 2009]. Such structures are widely interpreted to form by detachment faulting in areas of extension with relatively reduced magma supply [e.g., Buck *et al.*, 2005].

#### 4.2. Neovolcanic Terrain

The neovolcanic terrain occupies the central portion of the spreading axis, and can be clearly distinguished from the older BAB crust. It is dominated by high-amplitude backscatter intensity and categorized as hummocky, smooth, or sedimented. The “hummocky neovolcanic terrain” forms long, linear volcanic ridges at the center of the axial valley (axial volcanic ridges, or AVRs). Characteristic features include a high rugosity, highly variable slopes, and moderately high to high backscatter. This is interpreted to reflect multiple thick overlapping pillow and lobate flows with steep flow fronts, most likely formed by multiple diking events during phases of magmatic extension (Figure 3d) [e.g., Yeo *et al.*, 2012]. It is difficult to distinguish individual flows based only on backscatter (i.e., sediment cover) because of the surface roughness and numerous steep-sloped reflectors. However, an AUV *Sentry* photo survey from 2015 (dive 367, FK151121) [Resing and Shipboard Scientific Party, 2016] and ROV dives from 2016 (dive 9, EX1605L-1 [Gray, 2016]; dive S45, FK161129 [Butterfield *et al.*, 2017]) reveal both young and old pillow flows (Figures 3b and 3c). The hummocky volcanic terrain grades locally into “smooth neovolcanic terrain,” which is characterized by a low rugosity, low slopes, and high even backscatter. This is interpreted to represent flat-lying sheet flows that were erupted at a higher effusion rate, and is the dominant volcanic morphology in the southern segments where it comprises the main part of the ridge axis. In the central segments, smooth neovolcanic terrain generally occurs at the periphery of the hummocky flows near the axial valley walls and in deep basins. Seafloor observations during an AUV *Sentry* photo survey (dive 370, FK151121) [Resing and Shipboard Scientific Party, 2016] and ROV dives (dive 11, EX1605L-1; and dive S41, FK161129) [Gray, 2016; Butterfield *et al.*, 2017] near 17°N confirmed the presence of jumbled to ropy sheeted flows with minor lobate flows (Figures 3e and 3f) and numerous lava channels. “Sedimented neovolcanic terrain” also has a low rugosity and low slopes but is distinguished from the smooth volcanic terrain by a lower backscatter intensity. It occurs at variable distances from the hummocky AVRs within the broad axial valley, and fills in topographic lows around pillow mounds (Figure 3a).

#### 4.3. Volcanoes

Numerous volcanic edifices are found throughout the back-arc. These are classified as large rifted volcanoes, large volcanic cones, and smaller volcanic edifices. Only “small volcanic edifices” with diameters greater than 1 km were mapped; smaller edifices are numerous but difficult to distinguish from large hummocky mounds. The features that are clearly volcanoes are up to ~3 km in diameter and commonly have flat tops or dome shapes; obvious cones are less common. They have a clear circular shape and well-defined steep edges; some also have summit craters. They are common throughout the neovolcanic zone but also occur in hummocky old crust on the tops of the axial walls. “Large volcanic edifices” are ~4 to ~16.5 km in diameter, ~500 to ~2200 m in height, and have very high relief in addition to circular shapes and steep sides. Numerous off-axis examples can be seen at 13°0′N, and a particularly large cone occurs near the segment end at 16°20′N. A single large “rifted-volcano” near 17°N has a flat, circular morphology and is clearly split by the axial valley.

#### 4.4. Deep Sedimented Basins

Deep, sedimented basins separate the ridge segments along the shear zone offsets (SZOs) and nontransform discontinuities at the segment ends. Near the segment centers, sedimented basins are less common and only occur distal to the spreading axis. They are low depressions with smooth bottoms and low, even backscatter interpreted to represent thick sediment cover. The sediment cover is greatest in areas of low

magmatic activity at the segment ends and away from the narrow spreading center. Faulting is rare; where present, the basins are designated “faulted basins.”

#### 4.5. Structures

Features with strongly linear to curvilinear traces and scarps >100 m in height are identified as “major faults”; those with scarps <100 m high are referred to as “minor faults.” A total of 1664 major faults were measured with strike lengths of less than 100 m to a maximum of 8478 m; another 5148 minor faults were measured with strike lengths to a maximum of 11,540 m. Both are identified as highly reflective linear features in the backscatter data. All fault surfaces are moderately to steeply dipping (generally east-dipping on the west side of the back-arc segments and west-dipping on the east side) with apparent normal sense of movement. Some distinctive lineaments, interpreted to be eruptive fissures, occur along the AVRs. In the middle of each ridge segment, the lineaments all have similar strike directions, whereas at the segment ends they show many orientations, reflecting the structural complexity of the transfer zones.

### 5. Segment Geology

In this section, we describe the geology of 11 segments that comprise the active spreading center in the southern and central back-arc region (Figures 5–14). The mapped area includes two segments along the 124 km of the southern back-arc, and nine segments along 474 km of the central back-arc. The segments are named according to the latitude at the segment centers. For each segment, the cross-sectional morphologies are shown along profiles at the segment middle and end points. Structural azimuths are also examined, including major and minor faults and volcanic ridge axes.

#### 5.1. Southern Mariana Back-Arc

The southern Mariana back-arc between 11°50'N and 13°40'N was first described in detail by *Martínez et al.* [2000]. It is shallower than the central part of the back-arc (~3000 mbsl along the in the south, compared to ~3500–5000 m in the central back-arc), and the spreading axis approaches to within ~25 km of the presently active arc-front volcanoes, owing to the sharp westward curvature of the trench (Figure 2). The active spreading center is morphologically similar to a fast-spreading ridge, including a broad “inflated” zone with a narrow axial rise (the Malaguana-Gadao Ridge), a smooth flanking morphology, and a general lack of transform offsets, despite sharp changes in the trend of the spreading center (Figure 5). The presence of a shallow axial magma chamber along the Malaguana-Gadao Ridge was documented by *Becker et al.* [2010].

##### 5.1.1. The 12.8°N and 13.3°N Segments

The 12.8°N and 13.3°N segments are ~58 km in length and located ~25 km from the volcanic arc. They are morphologically similar and broadly symmetrical (low “skewness”), with widths of ~14–17 km, maximum seafloor depths of ~3400 to ~3700 mbsl (increasing northwards), and ~500–550 m-tall axial topographic highs (Figure 5; Table 1). Profile A-A' in Figure 5 shows topography similar to the fast-spreading EPR [cf., *MacDonald*, 2001]. At ~13°10'N (profiles B-B' and C-C' in Figure 5), clear valley walls up to 400 m high first appear and the axial zone bears a closer resemblance to the intermediate-rate spreading segments of the EPR [cf., *MacDonald*, 2001]. Along the spreading axis, the seafloor is dominated by heavily faulted but smooth and hummocky neovolcanic terrain. Minor sedimented neovolcanic terrain occurs along a narrow graben to the west of the spreading axis (Figure 5). The smooth flows are interpreted to represent the products of volcanic eruptions close to the center of the spreading axis, with the hummocky terrain on the flanks. The latter is thought to be dominated by lobate and pillow flows, possibly related to increased magma transport along lava tubes or greater eruptive volumes along faults on the eastern side of the back-arc spreading axis. The dominant structures along the 12.8°N segment have a mean orientation of  $39.3^\circ \pm 1.7^\circ$  (95% confidence interval;  $n = 325$ ; Figure 5). There is an abrupt change in the orientation at 13°4'N, where an OSC has an offset of ~4.6 km with the 13.3°N segment. The dominant structures along the 13.3°N segment have a mean orientation of  $23.8^\circ \pm 1.2^\circ$  ( $n = 488$ ; Figure 5). There are more outward-dipping faults on this segment, and individual faults have vertical throws of less than ~300 m.

#### 5.2. Central Mariana Back-Arc

Between ~13°40'N and 18°40'N, the central Mariana back-arc more closely resembles a slow-spreading (<50 mm yr<sup>-1</sup>) mid-ocean ridge. Segmentation is controlled by major SZOs, OSCs, and DEVALS. The axial valley is pronounced, with relief up to ~1500 m, with the highest relief at the segment ends. In cross-

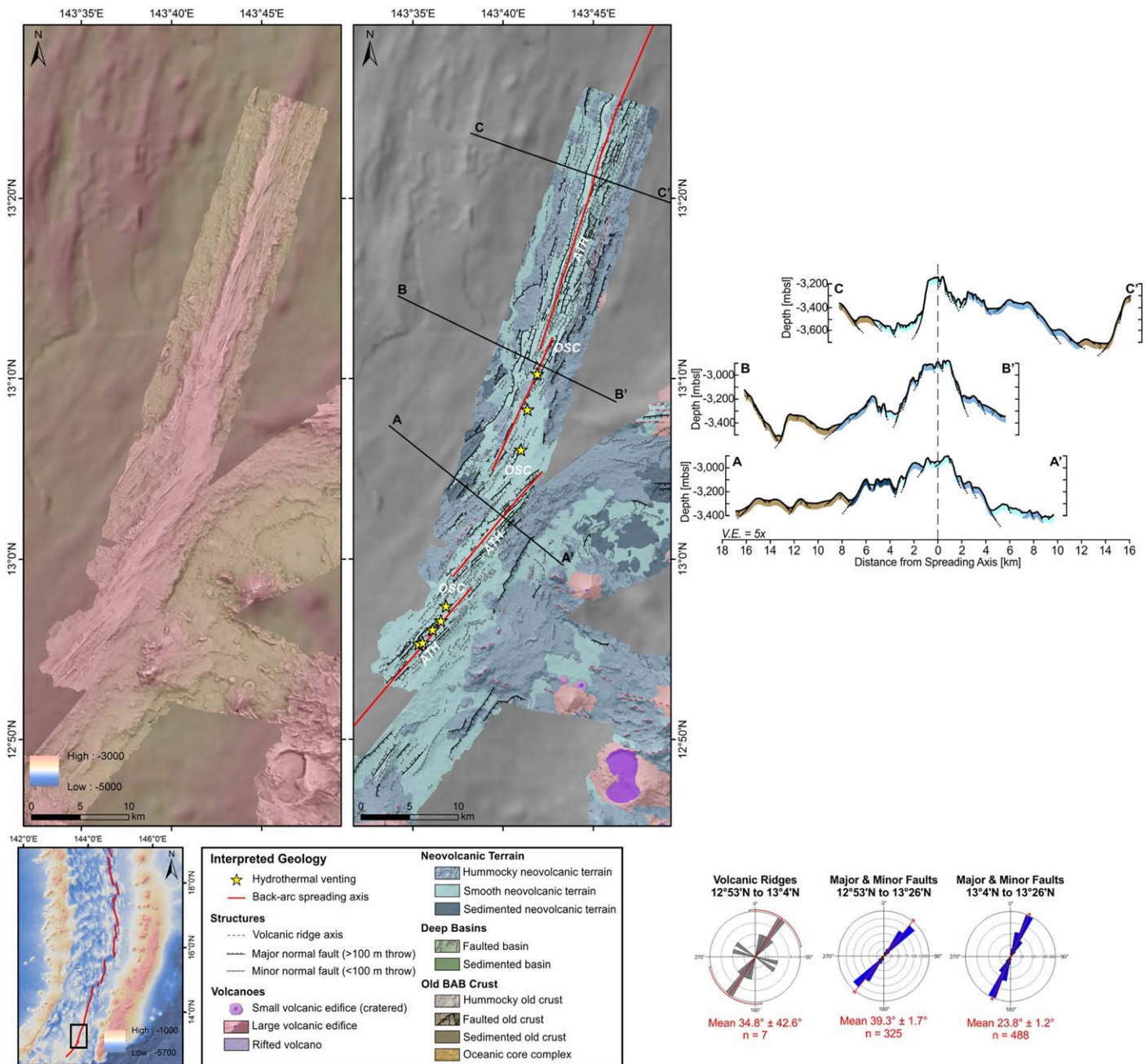


**Figure 5.** (left) Bathymetry, (middle) interpreted geological map, and (right) cross-axis profiles of the 12.8°N and 13.3°N segments, with the segment location in the back-arc shown as a black square in the lower left map. Azimuths of the major and minor faults from 12°53'N to 13°4'N, and 13°4'N to 13°26'N are shown in blue, and the volcanic ridge axes for the entire area are shown in grey (lower right corner). ATH = axial topographic high; OSC = overlapping spreading center; V.E. = vertical exaggeration (5×). A larger geological map is available in supporting information Figure S3.

section, the axial walls are highly skewed (i.e., have different heights on either side of the spreading center), and this skewness becomes more pronounced towards the segment ends. As noted by previous workers, the magmatic activity in this part of the back-arc is strongly focused at the segment centers [e.g., Fryer and Hussong, 1981; Hussong and Uyeda, 1981; Macdonald, 1982; Martínez et al., 2000]. The axial depths are greater than on mid-ocean ridge crust of the same age, a regional characteristic of the Mariana back-arc, and the orientations of faults are more variable with a wider zone of axial deformation, indicated by recent faulting far off-axis [Fryer and Hussong, 1981; Macdonald, 1982]. The axial zone of each segment is bound by heavily faulted old BAB crust along the valley walls. Hummocky neovolcanic terrain dominates the valleys,



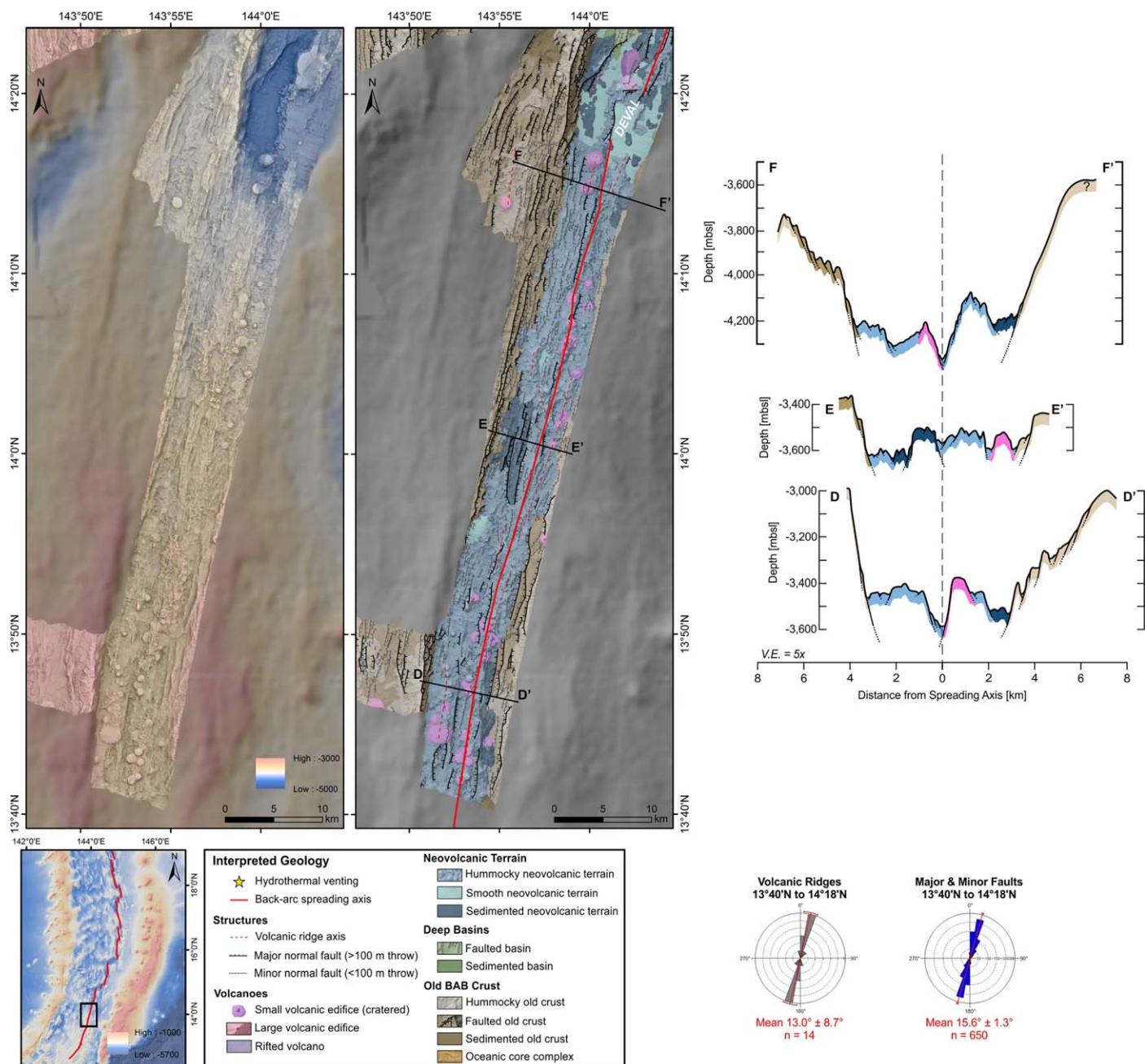


**Figure 6.** (left) Bathymetry, (middle) interpreted geological map, and (right) cross-axis profiles of the 13.9°N segment, with the segment location in the back-arc shown as a black square in the lower left map. Azimuths of the major and minor faults and the volcanic ridge axes for the entire segment from 13°40'N to 14°18'N are shown in blue and grey, respectively (lower right corner). DEVAL = deviation in axial linearity; V.E. = vertical exaggeration (5×). A larger geological map is available in supporting information Figure S4.

forming long volcanic ridges dotted by numerous small volcanic edifices. The axial zone is variably faulted, with individual segments dominated by either recent magmatic or tectonic extension.

### 5.2.1. The 13.9°N Segment

The 13.9°N segment is ~82 km in length and is located ~68 km from the volcanic arc. It is separated from the 13.3°N segment to the south by an OSC with an offset of ~1.8 km. The segment is characterized by a narrow (~8–13 km wide) axial valley bound by faulted old crust in the west and hummocky old crust in the east (Figure 6; Table 1). The valley relief ranges from ~550 in the south, ~250 m midway along its length, and ~700 m in the north, with a progressive northward deepening of the seafloor (3350 mbsl to 4300 mbsl; Table 1). The valley has a low degree of skewness in cross section with <100 m

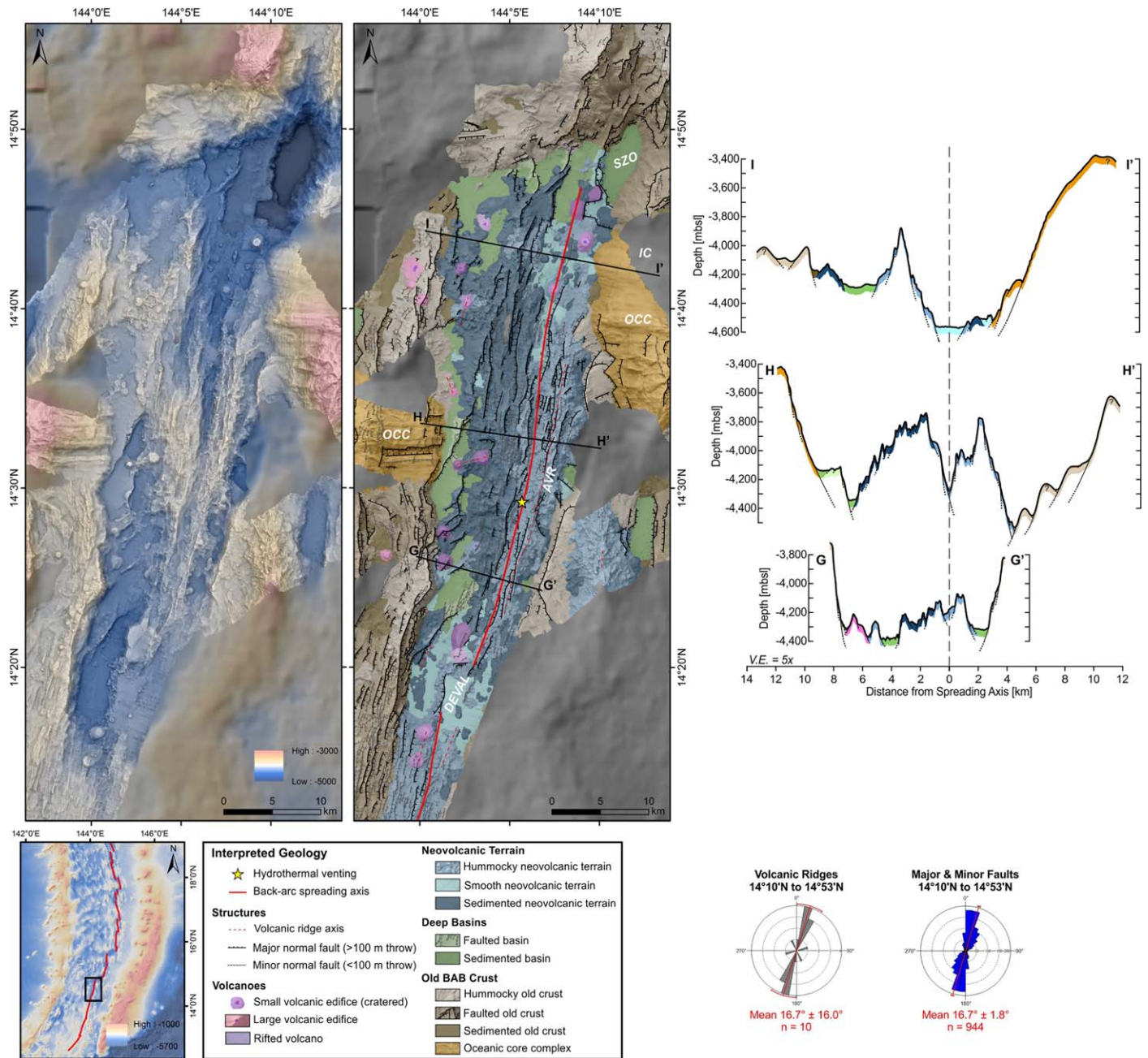


**Figure 7.** (left) Bathymetry, (middle) interpreted geological map, and (right) cross-axis profiles of the 14.5°N segment, with the segment location in the back-arc shown as a black square in the lower left map. Azimuths of major and minor faults and the volcanic ridge axes and for the entire segment from 14°18'N to 14°53'N are shown in blue and grey, respectively (lower right corner). AVR = axial volcanic ridge; DEVAL = deviation in axial linearity; IC = inside corner high; OCC = oceanic core complex; SZO = shear zone offset; V.E. = vertical exaggeration (5×). A larger geological map is available supporting information Figure S5.

height difference between the western and eastern walls (Figure 6; Table 1). The axial valley is dominated by hummocky and smooth neovolcanic terrain, with numerous small flat-topped volcanic edifices (Figure 6). Short volcanic ridges occur throughout the hummocky terrain. The lack of an axial volcanic high and the presence of a central graben (up to ~250 m deep) suggest a relatively low rate of magma supply (Figure 6). The total estimated volume of the neovolcanic products is ~334 km<sup>3</sup> (see supporting information for volume calculations). Intense faulting within the old crust and neovolcanic zone has a uniform orientation over the entire segment length of  $15.6^\circ \pm 1.3^\circ$  (n = 662). The maximum throw on the faults is ~400 m.



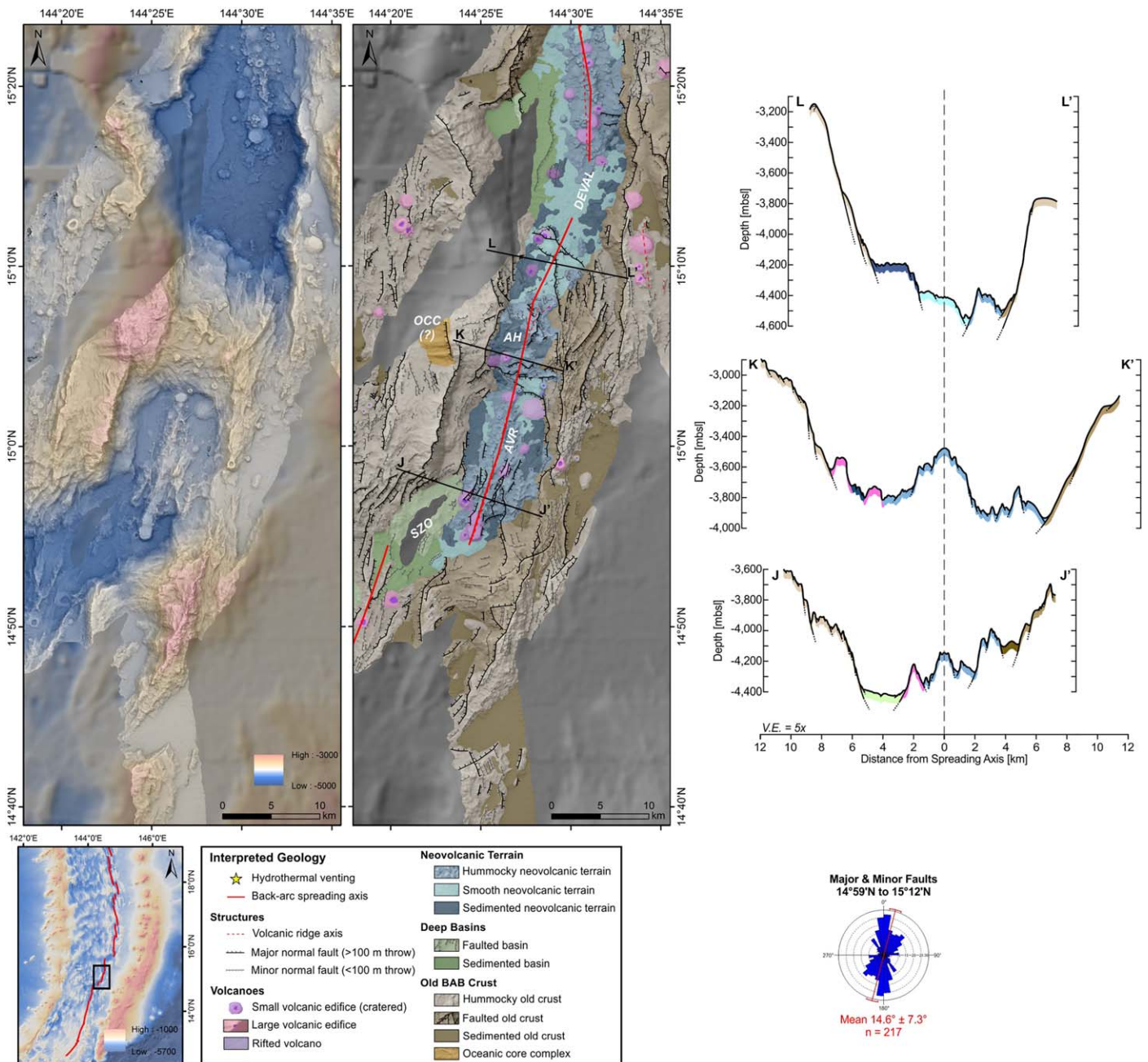


**Figure 8.** (left) Bathymetry, (middle) interpreted geological map, and (right) cross-axis profiles of the 15.1°N segment, with the segment location in the back-arc shown as a black square in the lower left map. Azimuths of the major and minor faults of the entire segment from 14°59'N to 15°12'N are shown in blue (lower right corner). AH = axial high; AVR = axial volcanic ridge; DEVAL = deviation in axial linearity; OCC(?) = possible oceanic core complex; SZO = shear zone offset; V.E. = vertical exaggeration (5×). A larger geological map is available in supporting information Figure S6.

### 5.2.2. The 14.5°N Segment

The 14.5°N segment is ~49 km long and located ~86 km from the volcanic arc, offset ~1 km to the east from the 13.9°N segment by a DEVAL. This segment is characterized by a northward deepening of the seafloor from ~4350 mbsl to a maximum depth of ~4550 mbsl and widening of the back-arc from ~12 to ~25 km (Figure 7; Table 1). The relief of the axial valley increases progressively from ~600 m in the south to ~1200 m in the north (Figure 7; Table 1). The ~1100 m high western flank of the axial valley wall at ~14°40'N is interpreted to be an inside corner high (IC) [e.g., *Severinghaus and Macdonald, 1988*] and oceanic core complex (as described in section 4.1; Figure 7; Table 1). An additional complex occurs on the opposite side of the axial valley, with rough corrugations parallel to the spreading direction, and N-S



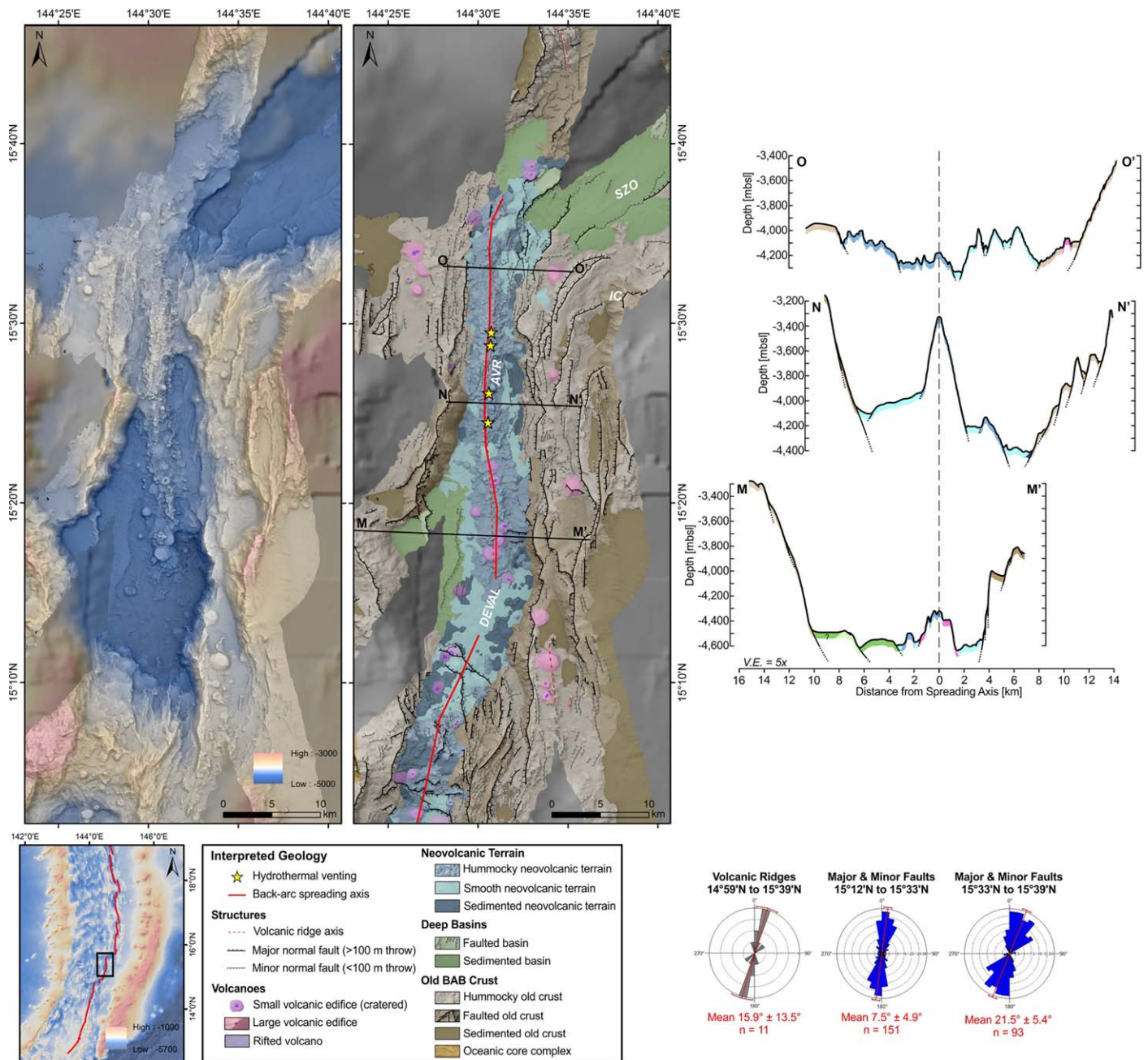


**Figure 9.** (left) Bathymetry, (middle) interpreted geological map, and (right) cross-axis profiles (right) of the 15.5°N segment, with the segment location in the back-arc shown as a black square in the lower left map. Azimuths of the major and minor faults from 15°12'N to 15°33'N, and 15°33'N to 15°39'N are shown in blue, and the volcanic ridge axes from 14°59'N to 15°39'N are shown in grey (lower right corner). AVR = axial volcanic ridge; DEVAL = deviation from axial linearity; IC = inside corner high; SZO = shear zone offset; V.E. = vertical exaggeration (5×). A larger geological map is available in supporting information Figure S7.

extension indicated by an 800 m wide E-W trending graben. These features confirm the formation of core complexes in the Mariana back-arc, following the earlier discovery of upper mantle peridotites in dredge samples at 20°N [Stern *et al.*, 1996]. They the second to be identified in a back-arc basin environment based on high-resolution bathymetric features, following the discovery of the Godzilla megamullion structures in the extinct Parece Vela basin [Ohara *et al.*, 2001]. The axial valley walls at this location are composed of heavily sedimented, faulted to hummocky old crust, and the basin floor is dominated by an 800 m high axial volcanic ridge. The heavily faulted neovolcanic terrain forming the ridge is clearly split along its axis forming a deep graben, with sedimented hummocky neovolcanic terrain in the west, and younger hummocky neovolcanic terrain to the east (Figure 7). Smooth neovolcanic terrain occurs only at the segment

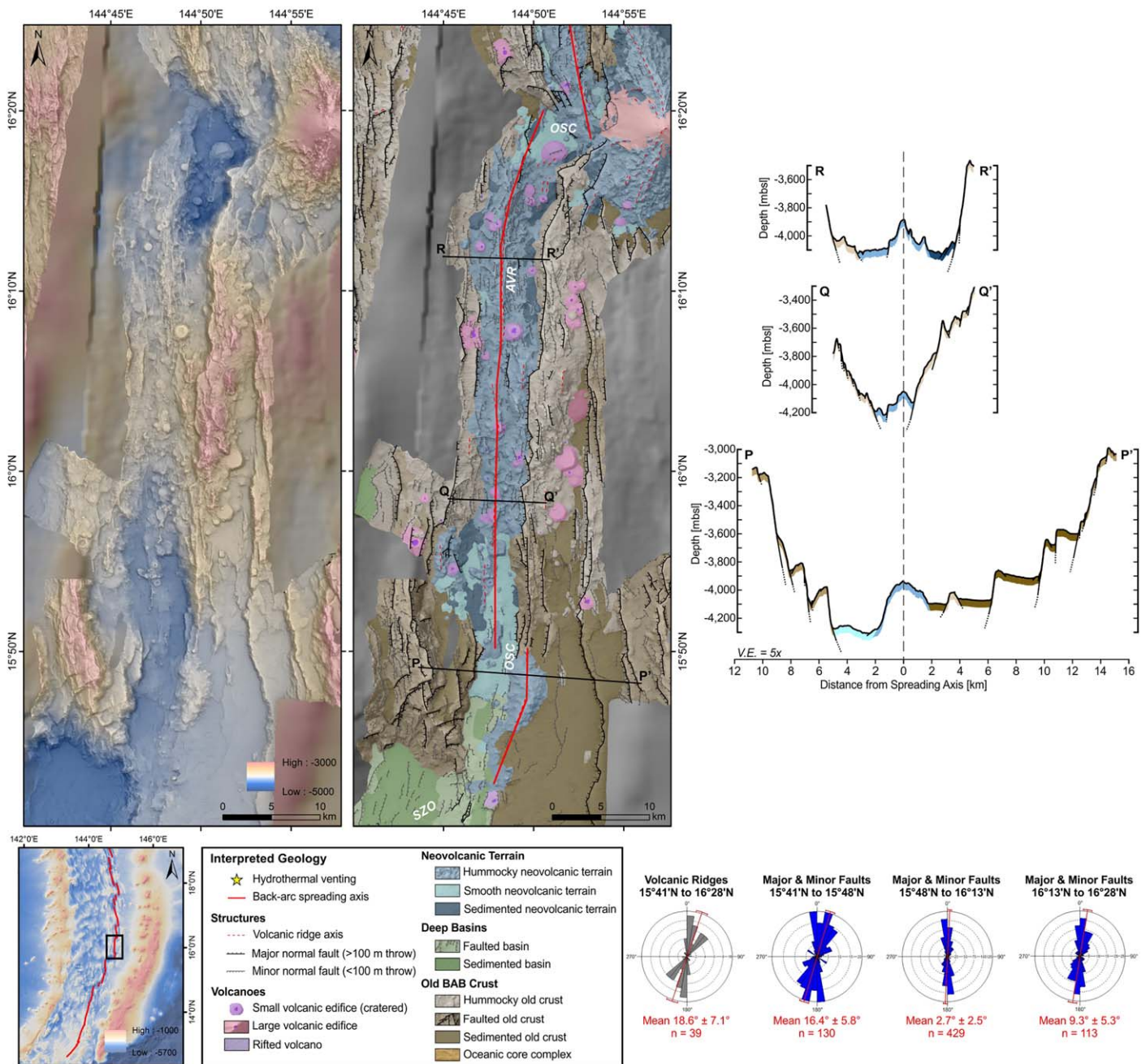


**Figure 10.** (left) Bathymetry, (middle) interpreted geological map, and (right) cross-axis profiles of the 16.1°N segment, with the segment location in the back-arc shown as a black square in the lower left map. Azimuths of the major and minor faults from 15°41'N to 15°48'N, 15°48'N to 16°13'N, and 16°13'N to 16°28'N are shown in blue, and the volcanic ridge axes for the entire segment are shown in grey (lower right corner). AVR = axial volcanic ridge; OSC = overlapping spreading center; SZO = shear zone offset; V.E. = vertical exaggeration (5×). A larger geological map is available in supporting information Figure S8.

ends. The volume of neovolcanic products in the axial valley is estimated to be  $\sim 271 \text{ km}^3$  (see supporting information). Fault orientations between 14°10'N and 14°53'N have a wide range with a mean of  $16.7^\circ \pm 1.8^\circ$  (n = 944), parallel to the volcanic ridges ( $16.7^\circ \pm 16.0^\circ$ , n = 10; Figure 7). A subset of faults trending  $\sim \text{ENE}$  forms a small graben at 14°30'N/144°0'E, consistent with a component of N-S extension (Figure 7). Individual fault throws along this segment are up to  $\sim 550 \text{ m}$  in height.

### 5.2.3. The 15.1°N Segment

The 15.1°N segment is  $\sim 33 \text{ km}$  long and located  $\sim 84 \text{ km}$  from the volcanic arc (Figure 8; Table 1). It is separated from the 14.5°N segment by a SZO comprising a series of deep sedimented basins in a



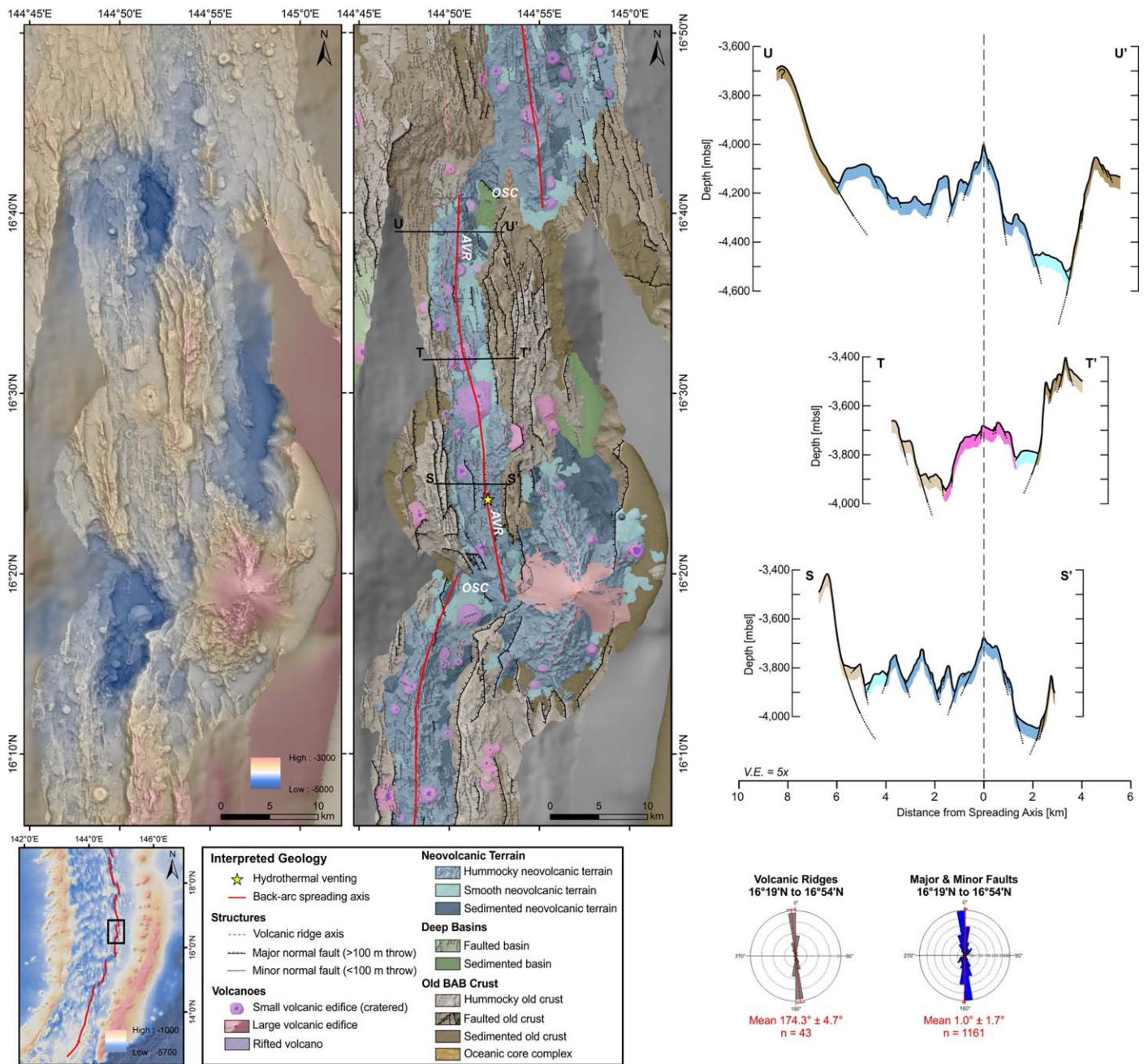


**Figure 11.** (left) Bathymetry, (middle) interpreted geological map, and (right) cross-axis profiles of the 16.5°N segment, with the segment location in the back-arc shown as a black square in the lower left map. Azimuths of the major and minor faults and the volcanic ridge axes for the entire segment from 16°19'N to 16°54'N are shown in blue and grey, respectively (lower right corner). AVR = axial volcanic ridge; OSC = overlapping spreading center; V.E. = vertical exaggeration. A larger geological map is available in supporting information Figure S9.

northeast-trending *en echelon* arrangement. The offset between the 15.1°N and 14.5°N segments is ~31 km, and is associated with a fracture zone that extends a further ~57 km to the west. The axial valley widens from ~17 to ~23 km midway along its length and narrows to ~13 km in the north, but the depth is similar to the 14.5°N segment, shallowing to ~3950 mbsl in the center (Figure 8; Table 1). The axial high is dominated by heavily faulted and sedimented hummocky neovolcanic terrain. In the southern portion of the segment, the neovolcanic zone is dominated by a narrow ~450 m tall hummocky axial volcanic ridge, with smooth and sedimented neovolcanic terrain toward the valley walls and sedimented basins (Figure 8). Axial valley relief increases northwards from ~800 to 1300 m, with approximately ~700 m difference in height in the northern part of the segment (Figure 8, Table 1). It has a documented



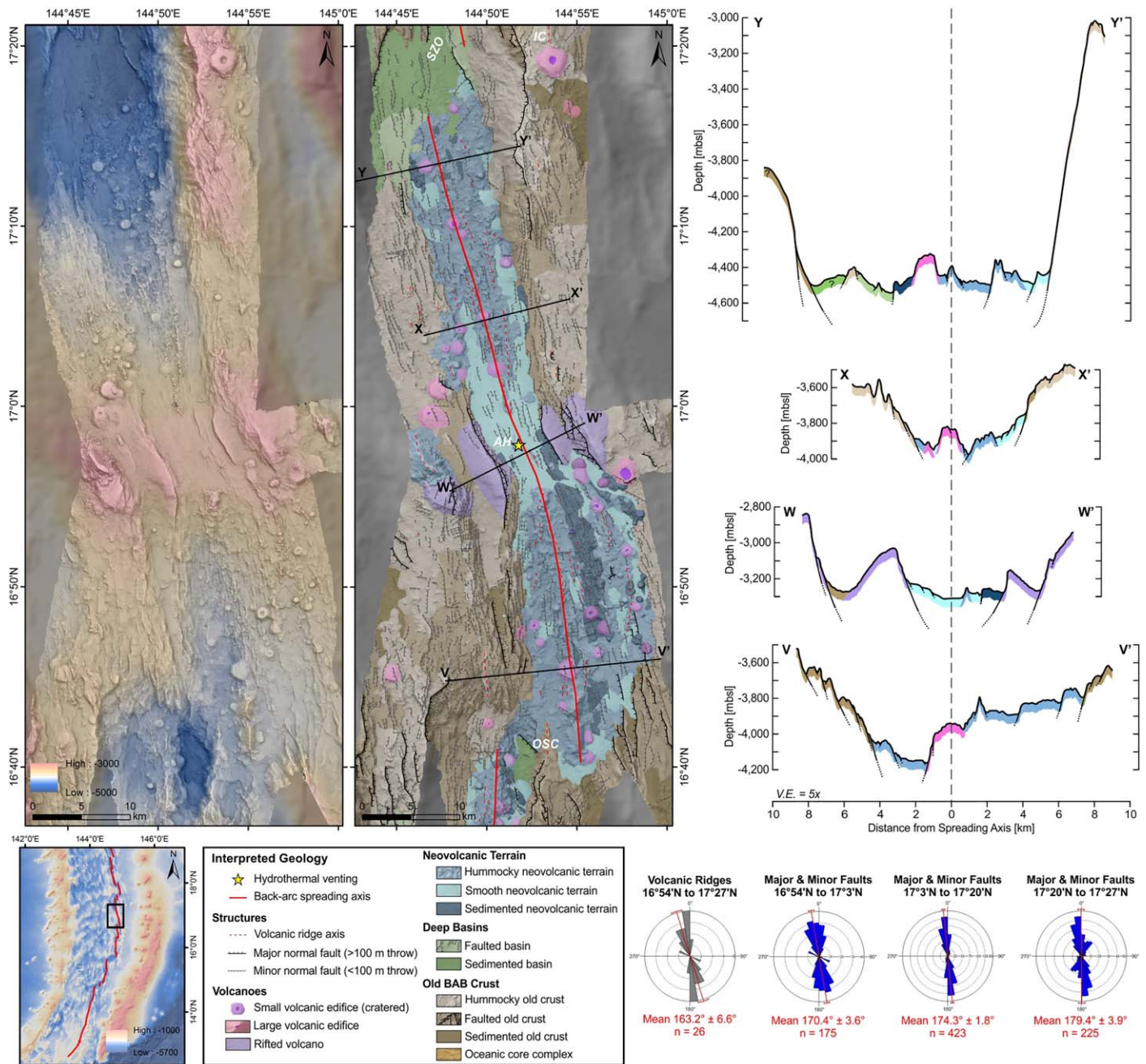


**Figure 12.** (left) Bathymetry, (middle) interpreted geological map, and (right) cross-axis profiles of the 17.0°N segment, with the segment location in the back-arc shown as a black square in the lower left map. Azimuths of the major and minor faults from 16°54'N to 17°3'N, 17°3'N to 17°20'N, and 17°20'N to 17°27'N are shown in blue, and the volcanic ridge axes for the entire segment are shown in grey (lower right corner). AH = axial high; IC = inside corner high; OSC = overlapping spreading center; SZO = shear zone offset; V.E. = vertical exaggeration (5×). A larger geological map is available in supporting information Figure S10.

spreading rate of  $\sim 40 \text{ mm yr}^{-1}$  [Kato et al., 2003]. The volume of neovolcanic products is estimated to be  $\sim 118 \text{ km}^3$  (see supporting information). The axial walls are dominated by hummocky old crust, which contains most of the faults, having a wide range of orientations (mean of  $14.6^\circ \pm 7.3^\circ$ ,  $n = 217$ ; Figure 8). The maximum throw on the faults is  $\sim 600 \text{ m}$ . Subordinate E-W and NW-SE trending faults are also present. Notably corrugated surfaces at  $15^\circ 8' \text{N}$  on the western side of the valley suggest the presence of another core complex. Of all the segments studied, the  $15.1^\circ \text{N}$  segment most closely resembles the slow-spreading MAR [e.g., near  $37^\circ \text{N}$ : MacDonal, 2001].

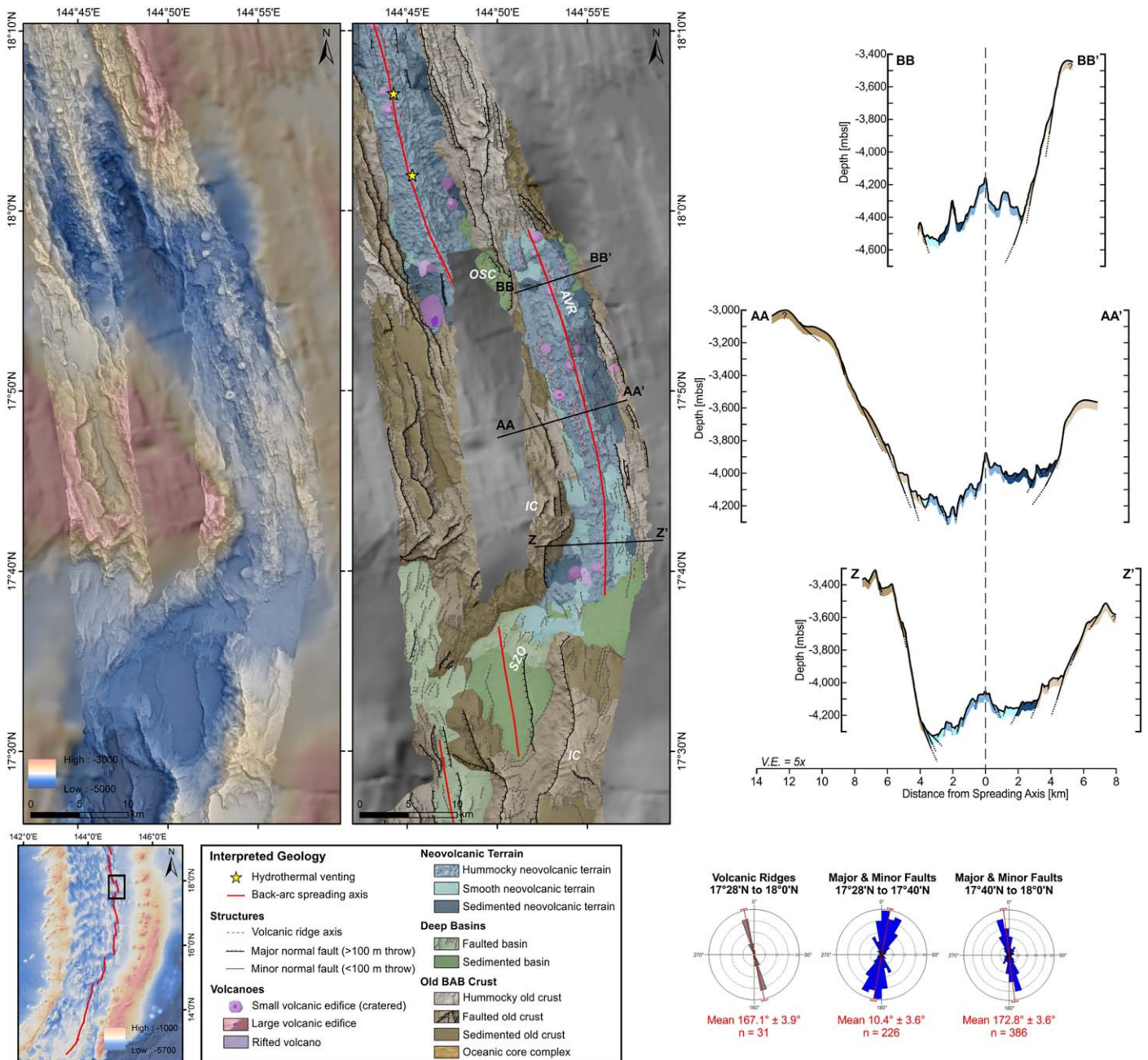


**Figure 13.** (left) Bathymetry, (middle) interpreted geological map, and (right) cross-axis profiles of the 17.8°N segment, with the segment location in the back-arc shown as a black square in the lower left map. Azimuths of the major and minor faults from 17°28'N to 17°40'N, and 17°40'N to 18°0'N are shown in blue, and the volcanic ridge axes for the entire segment are shown in grey (lower right corner). AVR = axial volcanic ridge; IC = inside corner high; OSC = overlapping spreading center; SZO = shear zone offset; V.E. = vertical exaggeration. A larger geological map is available in supporting information Figure S11.

### 5.2.4. The 15.5°N Segment

The 15.5°N segment is ~34 km long and located ~101 km from the volcanic arc. It is offset from the 15.1°N segment by an abrupt change in the trend of the spreading axis. The axial valley is ~22–25 km wide, shallowing northward from ~4650 to 4350 mbsl. The axial valley relief also decreases from ~1300 to 950 m (Figure 9; Table 1). There is a large height difference of ~400 m at the northeastern end of the segment forming an inside corner high (Figure 9; Table 1). The neovolcanic zone shows almost no faulting and has a tall axial volcanic ridge that rises up to ~1050 m above the surrounding seafloor (Figure 9). The ridge is composed of hummocky neovolcanic terrain surrounded by smooth and sedimented neovolcanic



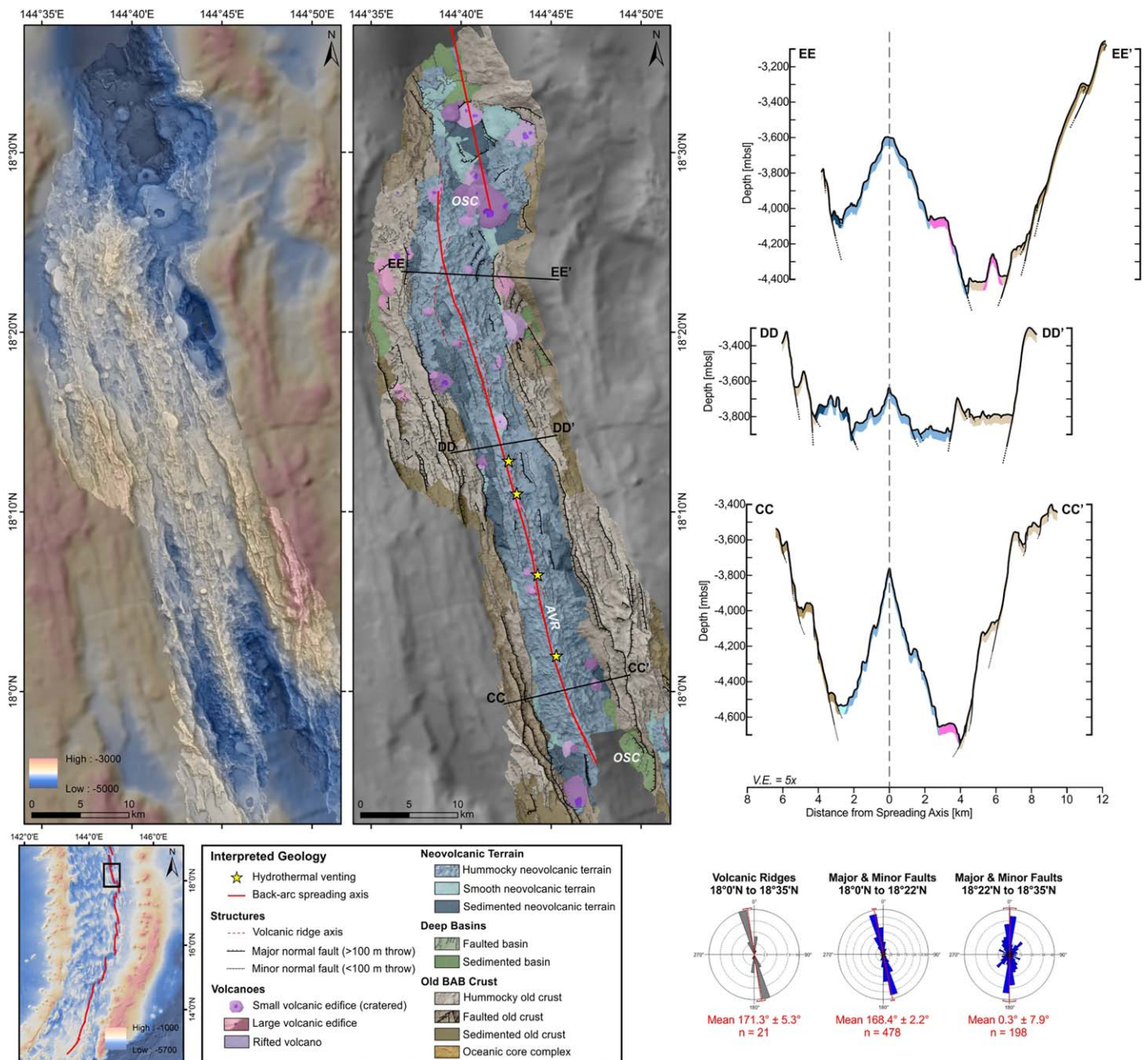


**Figure 14.** (left) Bathymetry, (middle) interpreted geological map, and (right) cross-axis profiles of the 18.2°N segment, with the segment location in the back-arc shown as a black square in the upper right map (lower left corner). Azimuths of the major and minor faults for 18°0'N to 18°22'N, and 18°22'N to 18°35'N are shown in blue, and the volcanic ridge axes for the entire segment are shown in grey (lower right corner). AVR = axial volcanic ridge; OSC = overlapping spreading center; V.E. = vertical exaggeration. A larger geological map is available in the supporting information Figure S12.

terrain (Figure 9; Table 1), with an estimated total volume of  $\sim 84 \text{ km}^3$  (see supporting information). An AUV *Sentry* photo survey (dive 367) conducted during the FK151121 cruise identified newly-erupted pillow lavas occupying an area 7.3 km long and 300–600 m in width at this spreading axis (Figure 3a) [Resing and Shipboard Scientific Party, 2016]. Two ROV *Deep Discoverer* dives (numbers 9 and 10) during cruise EX1605L-1 and one ROV *SuBastian* dive (number S45) during cruise FK161121 also found multiple generations of extensive pillow flows and minor lobate flows, and large steep-sided pillow mounds topped by smaller pillow mounds called “haystacks” (Figure 3b) [Gray, 2016; Butterfield et al., 2017]. The volcanic ridges along the axial valley have a mean orientation of  $15.9^\circ \pm 13.5^\circ$  (n = 151; Figure 9), whereas faulting

in the old BAB crust adjacent to the axial valley has a mean orientation of  $7.5^\circ \pm 4.9^\circ$  ( $n = 151$ ) with throws of up to 800 m.

#### 5.2.5. The 16.1°N Segment

The 16.1°N segment is  $\sim 64$  km long and located  $\sim 95$  km from the volcanic arc. It is offset  $\sim 35$  km to the east by a first-order ENE-trending SZO, associated with a fracture zone that extends for  $\sim 164$  km across the width of the back-arc. Like the other segments, it shallows northwards from  $\sim 4300$  to  $4100$  mbsl (Figure 10; Table 1). Axial relief also decreases northwards from  $\sim 1200$  to  $600$  m, with a height difference of  $300$ – $400$  m between the central and northern parts of the segment (Figure 10, Table 1). The entire segment has an hourglass-shape, with the axial zone being  $\sim 25$  km wide in the south,  $\sim 8$  km wide in the center, and  $\sim 10$  km wide in the north (Figure 10; Table 1). A discontinuous axial volcanic ridge,  $100$ – $350$  m in height, occupies an area of low relief at the center of the midsegment high (Figure 10). In the south, the axial volcanic ridge is slightly offset to the east where the valley widens near the SZO. The full spreading rate is  $\sim 35$  mm yr $^{-1}$  [Kato *et al.*, 2003], and the estimated volume of the neovolcanic products is  $\sim 163$  km $^3$  (see supporting information). The hummocky and smooth volcanics of the neovolcanic zone are moderately faulted, with throws of  $< 100$  m. Larger faults with throws of  $600$  m occur off-axis in the old crust between  $15^\circ 48'N$  and  $16^\circ 13'N$  and have an orientation of  $2.7^\circ \pm 2.5^\circ$  ( $n = 429$ ; Figure 10), although a number of faults and ridges with different orientation are related to the radial pattern of faulting at the base of a large off-axis volcanic cone (Figure 10). The axial walls are moderately faulted hummocky and sedimented old crust (Figure 10).

#### 5.2.6. The 16.5°N Segment

The 16.5°N segment is  $\sim 42$  km long and located  $\sim 97$  km from the volcanic arc. It is offset  $\sim 8.5$  km to the east from the  $16^\circ 20'N$  segment by a second-order OSC. A large volcanic cone occurs at the southern end of the segment to the east of the spreading center (Figure 11). The axial zone, which also has an hourglass shape, ranges from  $10$  km in width in the south to  $8$  km in the center and  $20$  km in the north (Figure 11; Table 1), shallowing from  $\sim 4050$  mbsl in the south to  $\sim 3950$  mbsl in the center, before rapidly deepening to  $\sim 4500$  mbsl in the north. In the south, the axial valley is  $\sim 650$  m deep and dominated by heavily faulted hummocky to smooth neovolcanic terrain with a  $\sim 300$  m-tall axial volcanic ridge (Figure 11; Table 1). Midway along the segment, the axial valley is  $\sim 500$  m deep and consists of unfaulted smooth volcanic terrain and large, dome-shaped volcanoes (Figure 11). In the north, it is  $\sim 1100$  m deep and contains a  $\sim 500$  m-tall axial volcanic ridge with minor faulting (Figure 11). The neovolcanic products along this segment have an estimated volume of  $\sim 108$  km $^3$  (see supporting information). Faulting between  $16^\circ 19'N$  and  $16^\circ 54'N$  trends  $\sim N-S$ , with a mean orientation of  $1.0^\circ \pm 1.7^\circ$  ( $n = 1161$ ); however, the mean orientation of the volcanic ridges is closer to  $174.3^\circ \pm 4.7^\circ$  ( $n = 43$ ; Figure 11). The irregular axial walls consist of hummocky to sedimented old crust.

#### 5.2.7. The 17.0°N Segment

The 17.0°N segment is  $\sim 70$  km and located  $\sim 103$  km from the volcanic arc. It is offset from the  $16.5^\circ N$  segment by an OSC, with a jump of  $\sim 8$  km. The segment has a pronounced hourglass shape, with the width of the axial zone ranging from  $\sim 19$  km in the south, to  $\sim 6$  km in the center, and  $\sim 18$  km in the north (Figure 12; Table 1). The axial valley is  $\sim 600$  m deep in the south with a seafloor depth of  $\sim 4150$  mbsl, shallowing to  $\sim 3300$  mbsl midway along the segment where the axial valley is  $\sim 450$  m deep. The orientation of the axial zone follows a gently sigmoidal shape, and then drops into a  $1500$  m deep valley at a water depth of  $\sim 4550$  mbsl in the north (Figure 12; Table 1). The southern neovolcanic zone occupies a broad area of un-sedimented hummocky and smooth volcanic flows separated by sedimented volcanic flows (Figure 12). The eastern half has higher backscatter intensity, suggesting that this area may be the location of a new spreading axis. This is supported by near-bottom side-scan surveys conducted in 2003 [Deschamps and Fujiwara, 2003; Deschamps *et al.*, 2004; Deschamps *et al.*, 2005; Asada *et al.*, 2007]. There are abundant minor faults within the axial valley, but mainly within the sedimented flows and near the basin walls. The central part of the neovolcanic zone is characterized by a large, split flat-topped volcano (Figure 12). Further away from the spreading center, a second split volcano is mirrored on either side of the axial valley, indicating multiple episodes. A magma lens was imaged at this location at  $\sim 4$  km depth in multichannel seismic surveys [Taylor *et al.*, 2002], and the site was visited by submersible in 2008 [Fujiwara *et al.*, 2008]. It was also the focus of an AUV *Sentry* photo survey during dive 370 in 2015 [Resing and Shipboard Scientific Party, 2016], and ROV dives in 2016 [Gray, 2016; Butterfield *et al.*, 2017]. The center of the volcano is smooth and unfaulted, and multiple ROV dives revealed extensive jumbled and ropey sheet flows and minor lobate flows, indicating



high effusion rates (Figures 3e and 3f). This smooth seafloor morphology is in sharp contrast to the other segments of the central back-arc, which are dominated by hummocky axial volcanic ridges. *Fujiwara et al.* [2008] observed almost no sediment in the axial portion, and our data show a decrease in backscatter intensity toward the eastern wall. In the northern part of the segment, the axial valley is dominated by hummocky neovolcanic terrain along discontinuous low-relief volcanic ridges with little faulting; smooth neovolcanic terrain occurs at the flanks (Figure 12a). The overall spreading rate of the segment is  $\sim 30 \text{ mm yr}^{-1}$  [Kato et al., 2003], and the estimated volume of material within the neovolcanic zone is  $\sim 474 \text{ km}^3$  (see supporting information). The axial valley walls are dominated by hummocky old crust, with minor faulting (throws  $< 100 \text{ m}$ : Figure 12). Between  $17^{\circ}3'N$  and  $17^{\circ}20'N$ , faults have a mean orientation of  $174.3^{\circ} \pm 1.8^{\circ}$  ( $n = 423$ ; Figure 12). Between  $17^{\circ}20'N$  and  $17^{\circ}27'N$ , fault orientations are variable (mean of  $179.4^{\circ} \pm 3.9^{\circ}$ ,  $n = 225$ ; Figure 12), reflecting the shape of the spreading axis. North of  $17^{\circ}20'N$ , an inside-corner high on the eastern flank of the valley is dominated by a large detachment fault ( $\sim 22^{\circ}$  dip) with a maximum throw of  $\sim 3000 \text{ m}$  (Figure 12).

#### 5.2.8. The $17.8^{\circ}N$ Segment

The  $17.8^{\circ}N$  segment is  $\sim 39 \text{ km}$  long and located  $\sim 97 \text{ km}$  from the volcanic arc (Figure 13; Table 1). This segment marks the apex of the curved subduction zone, where the back-arc is the widest. It is separated from the  $17.0^{\circ}N$  segment by another SZO, with a total offset of  $\sim 42 \text{ km}$  to the east. This offset is associated with the extensive Pagan Fracture Zone, which extends  $\sim 226 \text{ km}$  westward across the width of the back-arc and reflects the curvature of the arc, which changes from NE-SW to  $\sim N-S$  (Figure 2). The segment widens and deepens northward, from  $\sim 15$  to  $17 \text{ km}$  in width and from  $\sim 4300$ – $4650 \text{ mbsl}$  (Figure 13; Table 1). The axial valley walls increase in height from  $\sim 1000$  to  $1300 \text{ m}$ , with a  $\sim 550 \text{ m}$  height difference (“skewness”) between the eastern and western axial walls in the central portion of the segment (Figure 13; Table 1). The old crust that forms the walls is heavily faulted on the west and dominated by hummocky volcanics in the east. A narrow hummocky axial volcanic ridge up to  $500 \text{ m}$  high occurs within the neovolcanic zone, surrounded by sedimented and smooth neovolcanic terrain (Figure 13). The total volume of neovolcanic products is estimated to be  $\sim 83 \text{ km}^3$  (see supporting information). Between  $17^{\circ}40'N$  and  $18^{\circ}0'N$ , the major and minor faults have a mean orientation of  $172.8^{\circ} \pm 3.6^{\circ}$  ( $n = 386$ ; Figure 13). The volcanic ridges follow the dominant fault orientation, with a mean orientation of  $167.1^{\circ} \pm 3.9^{\circ}$  ( $n = 31$ ; Figure 13).

#### 5.2.9. The $18.2^{\circ}N$ Segment

The  $18.2^{\circ}N$  segment is  $\sim 61 \text{ km}$  long and located  $\sim 113 \text{ km}$  from the volcanic arc. It is separated from the  $17.8^{\circ}N$  segment by an OSC with a total offset of  $\sim 9 \text{ km}$  to the west and occupies the widest part of the Mariana back-arc. The segment morphology has been described previously by *Asada et al.* [2007], and the early discovery of hydrothermal activity along this segment (Alice Springs vent field) made it the target of several investigations. It ranges in width from  $\sim 16 \text{ km}$  at the segment ends to  $\sim 14 \text{ km}$  in the segment center (Figure 14; Table 1), and it has a spreading rate of  $\sim 25 \text{ mm yr}^{-1}$  [Kato et al., 2003]. This is the shallowest segment of the central back-arc, at  $3900 \text{ mbsl}$ , with an axial valley relief of  $\sim 600 \text{ m}$ , deepening to  $4400 \text{ mbsl}$  in the south and  $4750 \text{ mbsl}$  in the north (Figure 14; Table 1). Along the southern half of the spreading segment, the axial zone is dominated by an unfaulted volcanic ridge,  $800$ – $950 \text{ m}$  in height, comprised of hummocky volcanic terrain (Figure 14). Along the northern half of the axial zone, there is increased faulting and abundant sedimented neovolcanic terrain with a narrow hummocky volcanic ridge that is  $200 \text{ m}$  in height (Figure 14). The total volume of neovolcanic material is estimated to be  $\sim 401 \text{ km}^3$  (see supporting information). Between  $18^{\circ}0'N$  and  $18^{\circ}22'N$ , the faults have a narrow range of orientations with a mean of  $168.4^{\circ} \pm 2.2^{\circ}$  ( $n = 478$ ; Figure 14), similar to the volcanic ridges ( $171.3^{\circ} \pm 5.3^{\circ}$ ,  $n = 21$ ).

## 6. Regional Structures

The regional bathymetry (GMRT v3.2) [Ryan et al., 2009] and the vertical gravity gradient [Sandwell et al., 2014] reveal the major structural lineaments throughout the back-arc (Figure 15a). The heavily block-faulted terrain described by previous authors that characterizes most of the back-arc bears a close resemblance to the abyssal hill fabric of slow-spreading mid-ocean ridges. The southern back-arc has fewer lineaments overall, transitioning from relatively smooth terrain over much of its width to block-faulted terrain toward the remnant arc in the west (near  $143^{\circ}0'E$  at  $13^{\circ}30'N$ ; Figure 15). A series of N-S trending lineaments in the southern half of the back-arc, which are characterized by deep sub-parallel valleys (Figure 15a), are also seen in the northern half of the back-arc where they turn toward NW-SE, following the orientation of the

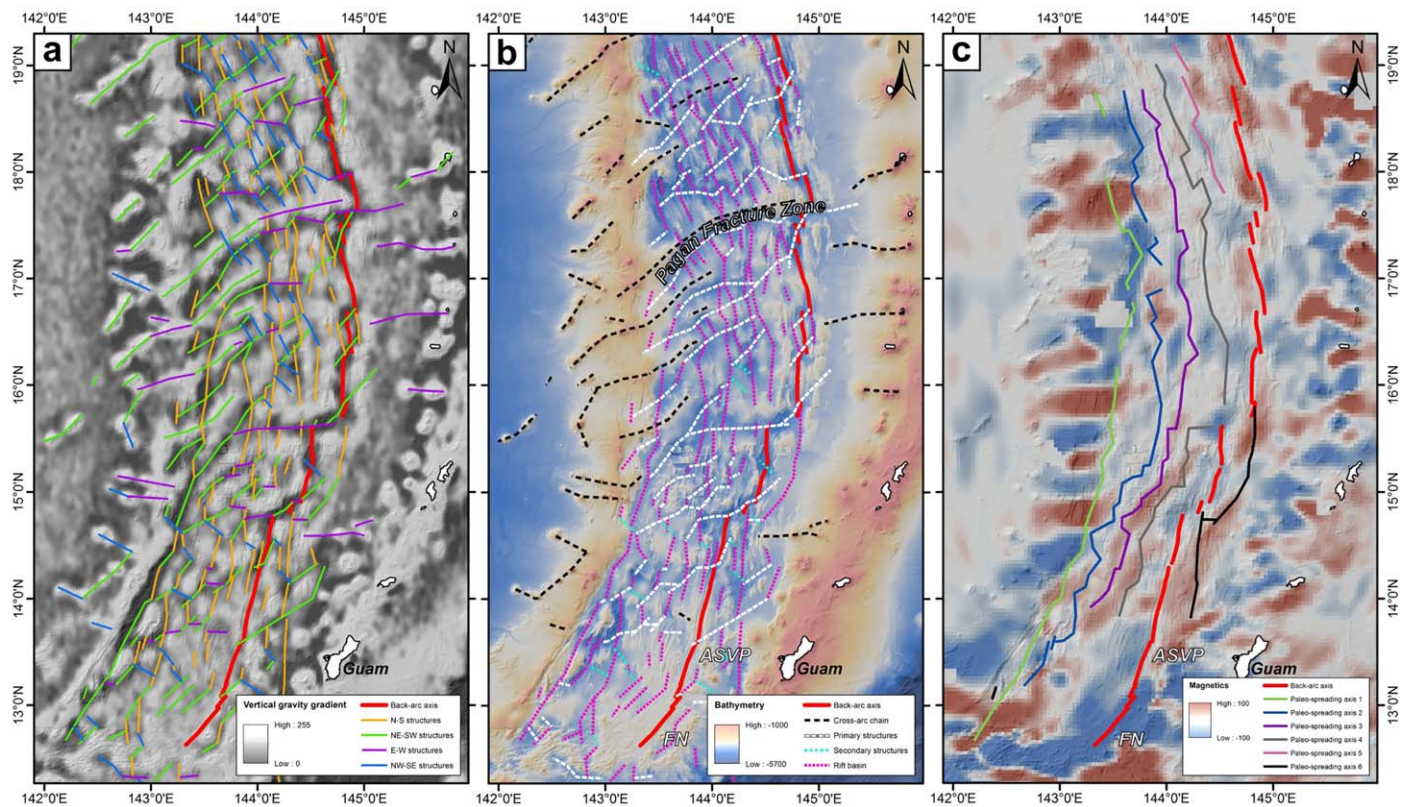


**Figure 15.** Regional structural interpretation of the Mariana back-arc: (a) lineaments classified according to orientation, interpreted from the vertical gravity gradient (50% transparency) [Sandwell *et al.*, 2014] overlain on hill-shaded bathymetry; (b) interpretation of structures, with the regional bathymetry (GMRT v.3.2) [Ryan *et al.*, 2009]; and (c) paleo-spreading axes interpreted from continuous rift basins that broadly coincide with magnetic anomalies, with the 2-arc min Earth Magnetic Anomaly Grid (50% transparency) [Maus *et al.*, 2009] overlain on hill-shaded bathymetry. Subaerial volcanoes are shown in white. ASVP = Alphabet Seamount Volcanic Province; FN = Fina Nagu volcanic complex.

volcanic front. Both the N-S and NW-SE lineaments are interpreted to be rift basins formed during back-arc opening (Figure 15b). Cross-cutting these structures are major E-W and NE-SW trending lineaments (Figure 15a), which include deep, linear valleys as well as topographic highs. The valleys are interpreted to be ancient transform faults (primary structures), several of which extend across the basin, including major fracture zones at 15.6°N and 17.5°N (the Pagan Fracture Zone; Figure 15b). Secondary structures are not as well developed as the primary structures (which are distinct linear features), and do not appear to cross-cut other structures (Figure 15b). The topographic highs that follow this orientation are thought to be related to cross-arc volcanic chains described briefly by Oakley *et al.* [2009] (Figure 15b). These cross-arc chains are heavily faulted across most of the back-arc, with discrete volcanoes observed only along the cross-arc chains closest to the active volcanic arc (including the Guguan, Diamante, and Pagan cross-arc chains) [Stern *et al.*, 2006; Stern *et al.*, 2014] and those that extend westward from the remnant arc (Figure 15b).

Magnetic anomalies visible in the global 2-arc min Earth Magnetic Anomaly Grid [Maus *et al.*, 2009] reveal linear features that are subparallel to the active spreading center (Figure 15c). These anomalies broadly correlate with several nearly continuous rift basins and may represent paleo-spreading centers formed as the back-arc rifting “jumped” progressively eastward [e.g., Fryer, 1981]. The strongest magnetic anomaly closely follows the present-day spreading axis between 20°0’N and ~15°40’N. South of ~15°40’N, this anomaly is located east of the spreading axis (Figure 15c), suggesting that the spreading axis at this location has recently jumped westward, in contrast to the general evolution of the back-arc. Abandoned rift valleys are clearly visible in the bathymetry along this magnetic anomaly, further supporting the interpretation as a paleo-spreading center (supporting information Figure S13). South of 13°40’N, a cluster of near-arc volcanoes (the Alphabet Seamount Volcanic Province) formed on young (Late Neogene) thin back-arc crust where the arc magmas appear to have exploited an earlier back-arc structure [Stern *et al.*, 2013]. The increased magmatism in this part of the southern back-arc, the westward rift jump of the southern back-arc



spreading axis, and the reorganization of the southern arc volcanoes appear to be closely related to the separate and complex evolution of the southern termination of the Mariana arc [cf., Stern *et al.*, 2013].

## 7. Discussion

### 7.1. Large-Scale Segmentation and Cross-Arc Structures of the Mariana Back-Arc

The eastward migration of the Mariana trench relative to the Philippine Sea plate has resulted in sinistral shearing in the southern and central back-arc that is accommodated by three major shear zone offsets at 14.8°N, 15.6°N, and 17.5°N (Figure 15). These discontinuities offset the ridge segments by 31–42 km each. At 14.8°N and 17.5°N, sinistral shearing is accommodated by short  $\sim$ N-S-trending faults producing a series of *en echelon* trench-parallel basins (Figures 16a and 16c). Along the 14.8°N SZO, the eastward-stepping basins trend  $\sim$ 3–24°, are  $\sim$ 10–12 km long,  $\sim$ 4–8 km wide,  $\sim$ 2.5–6 km apart, and reach depths of over 5000 mbsl. Along the 17.5°N SZO, the eastward-stepping basins trend  $\sim$ 349–351°, are  $\sim$ 14–20 km long,  $\sim$ 7–8 km wide,  $\sim$ 3 km apart, and reach depths of over 4900 mbsl. This type of faulting is common in propagating rifts [e.g., Einarsson and Eiríksson, 1982; Sigmundsson, 2006] and likely results from the asymmetry of the back-arc opening. The deep, magma-starved sedimentary basin corresponding to the 15.6°N SZO ( $\sim$ 30 km long and reaching depths of over 4600 mbsl; Figure 16b) also appears to be related to left-lateral shearing. This style of ridge segmentation contrasts with the first-order discontinuities that characterize the global mid-ocean ridge system, which may offset segments by hundreds of kilometers [Macdonald *et al.*, 1982]. Smaller-offset discontinuities are common between the slow-spreading MAR [e.g., Schouten *et al.*, 1985] and the Mariana back-arc, which contains at seven second-order OSCs and DEVALs in the study area. The overlap between segments includes both along-axis gaps (negative offsets) and true overlaps up to  $\sim$ 9 km. In the central segments, OSCs are associated with oblique extensional faulting with segment ends pointing slightly toward each other. In contrast, OSCs in the southern back-arc are characterized by abrupt changes in the orientations of the spreading axis. This may be due to the thermal structure of the segments and the relative importance of magmatic versus tectonic extension [Grindlay *et al.*, 1991].

Oakley *et al.* [2009] proposed a model of magmatic segmentation for the Mariana back-arc in which cross-arc volcanic chains have acted as focal points for magmatism and nucleation of back-arc segments. However, not every segment center is associated with a clearly defined cross-arc chain of volcanoes. Instead, the cross-arc chains that cross the entire width of the back-arc (not just the volcanically active portions that extend westward from the arc; shown as black dashed lines in Figure 15b) are parallel to major E-W and NE-SW trending structures (shown as white dashed lines in Figure 15b), indicating that these structures were probably conduits for increased volcanism at the seafloor. Similar cross-arc chains that extend westward from the remnant West Mariana Ridge are colinear with NNE-trending fractures in the Parece Vela Basin, and generally appear to follow the same structural trend (supporting information Figure S14). These observations suggest that the cross-arc chains follow long-lived basement structures, inherited from or even pre-dating successive back-arc opening episodes [Fryer and Hussong, 1982; Fryer, 1995]. Zhang *et al.* [2016] considered that transform faults in the South China Sea, Okinawa Trough, West Philippine Basin, and Shikoku-Parece Vela basins are similarly inherited structures, the highly oblique orientation of which reflects complex plate convergence and rotation. Thus, the segmentation of the Mariana back-arc spreading center may be controlled by an early fabric in the arc crust, with all of the major and minor offsets associated with a major E-W or NE-SW trending structures at the regional scale (Figure 15b). These preexisting structures may also have influenced the locations of volcanoes along the island arc, as suggested by Fryer [1995].

### 7.2 Segment-Scale Fault Patterns and Spreading Direction

Segment-scale faulting in the back-arc region closely follows the regional structural trends, in particular the curvature of the subduction zone from south to north along the length of the arc. Some segments are undergoing nearly pure extension while others show a strong component of oblique extension. However, axis-perpendicular extension is dominant, allowing precise spreading directions to be determined.

On the southern segments (12.8°N, 13.3°N, and 13.9°N), the faulting is remarkably consistent between the neovolcanic zone and the valley bounding faults, both dominated by almost pure extension. The spreading directions are  $129.3^\circ \pm 1.7^\circ$  along the 12.8°N segment,  $113.8^\circ \pm 1.2^\circ$  along the 13.3°N segment, and  $105.6^\circ \pm 1.3^\circ$  along the 13.9°N segment, perpendicular to the measured faulting. At 14.5°N, the spreading direction is

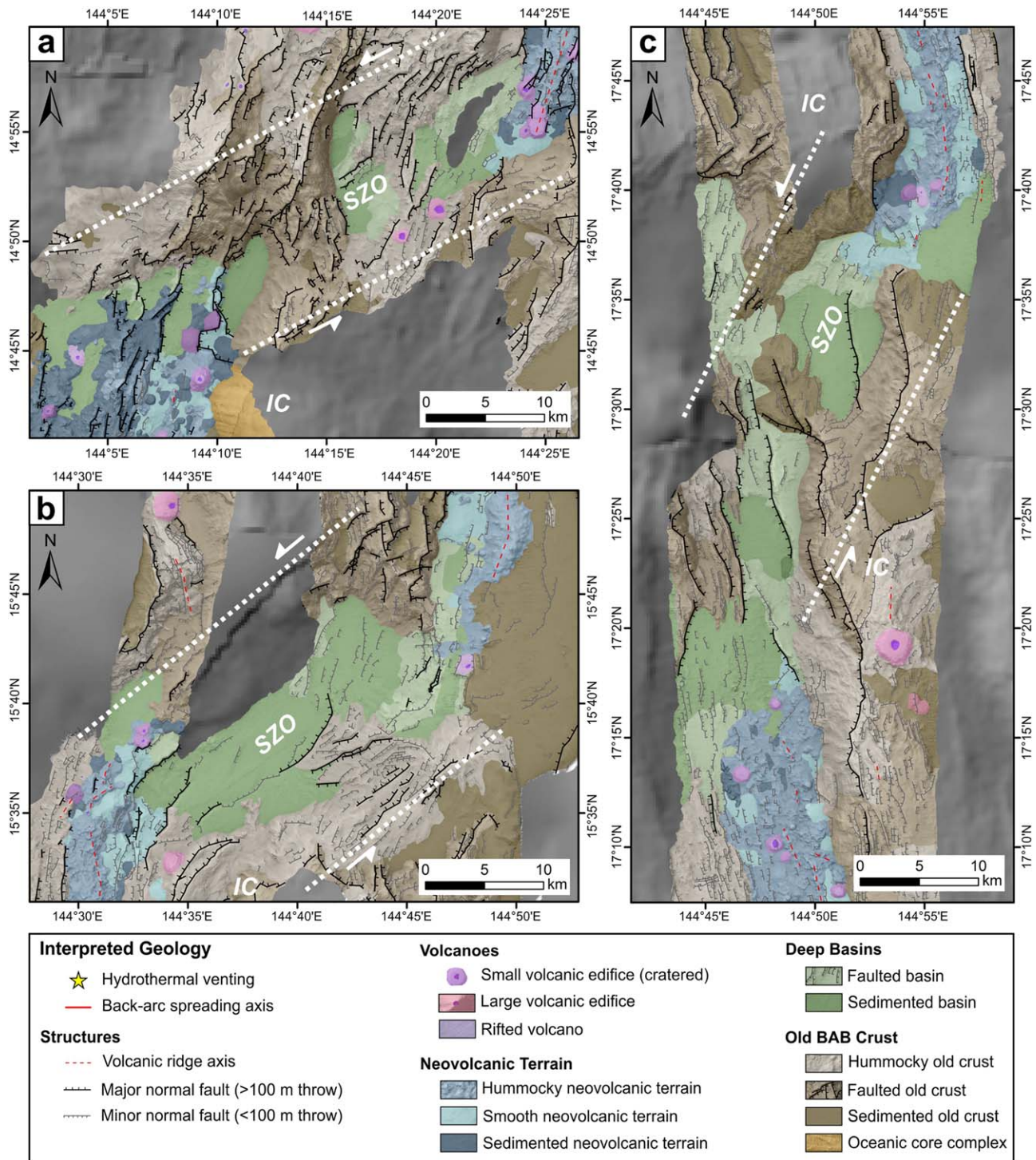


**Figure 16.** Structures and interpreted geology of the major shear zone offsets along the spreading axis, highlighting the sinistral shear components with orientations indicated by dotted white lines and arrows: (a) the 14.8°N SZO with a general trend of ~61°; (b) the 15.6°N SZO with a general trend of ~51°, and (c) the 17.5°N SZO with a general trend of ~21°. These offsets are associated with major fracture zones that extend westward across the back-arc (Figure 15). IC = inside corner high; SZO = shear zone offset.

106.7 ± 1.3°, but the faults show an anastomosing pattern, and there is a subset of ~E-W-trending faults that appear to be associated with N-S extension. The latter form a graben at 14°30'N/144°0'E (Figure 7), near which small volcanic edifices are aligned in the E-W faulting direction. At 15.1°N, the spreading direction is 104.6 ± 7.3° but with a large uncertainty related to minor left-lateral shearing of the segment and



displacements in the spreading axis. This complexity decreases northward and disappears along the 15.5°N segment where there is a notable lack of faulting within the neovolcanic zone and the spreading direction is  $97.5^\circ \pm 4.9^\circ$ .

On the central segments (16.1°N, 16.5°N, and 17.0°N), the faults show increasing curvature and evidence of oblique offsets. The spreading direction is  $92.7^\circ \pm 2.5^\circ$  at 16.1°N but then shifts progressively from  $91.0^\circ \pm 1.7^\circ$  at 16.5°N to  $80.4^\circ \pm 3.6^\circ$  in the southern part of the 17.0°N segment and  $84.3^\circ \pm 3.9^\circ$  in the northern part of the 17.0°N segment. As noted by *Deschamps et al.* [2005], the faulting in the center of the 17.0°N segment is oblique to the distal faults and abyssal hill fabric, which trend ~N-S. This is thought to reflect an early episode of spreading that was dominantly E-W followed by a shift to the present orientation at ~1 Ma. Geodetic measurements indicate that the whole of the basin along 17.0°N segment has been widening in a direction of ~73° [*Kato et al.*, 2003; *Deschamps et al.*, 2005], but local spreading is clearly oblique to that opening. This may be explained by a hot magmatic center that has responded more quickly than the cold segment ends [*Deschamps et al.*, 2005]. The spreading directions along the 17.8°N and 18.2°N segments are  $82.8^\circ \pm 3.6^\circ$  and  $78.4^\circ \pm 2.2^\circ$ , respectively.

### 7.3 Axial Morphology and Magma Supply Rates

The morphology of the southern Mariana back-arc bears a strong resemblance to fast-spreading mid-ocean ridges, despite its slow spreading rate. *Martínez et al.* [2000] proposed several mechanisms that could account for the enhanced magmatism: (1) trench-parallel extension and inward-radiating faulting that reflects the geometry of the trench; (2) decoupling of the spreading centers from the regional stress field affecting the eastern flank of the basin; and (3) input of arc magmas from the nearby volcanic front [*Fryer*, 1995; *Fryer et al.*, 1998]. The latter is supported by geochemical studies that indicate an arc component in the Alphabet Seamount Volcanic Province (ASVP) [*Fryer et al.*, 1998; *Stern et al.*, 2013] and the Fina Nagu volcanic complex [*Brounce et al.*, 2016]. The contribution of arc magmas may also explain the thicker crust and shallower depth of the southern back-arc [*Martínez et al.*, 2000]. New mapping shows a gradual transition from a “fast-spreading” morphology in the south to an “intermediate-spreading” morphology farther north, with pronounced axial valley walls first appearing at ~13°20'N. At 13°40'N, there is a sudden increase in the distance to the volcanic front of the arc and the development of a “slow-spreading” morphology. Distinctive mid-segment highs are evident, with narrow (8–13 km wide), deep axial valleys, and the farther away from the arc, the deeper the axial valley becomes. These observations support a model of decreasing influence of arc-enhanced magmatism in the central back-arc.

The eruption style, degree of faulting, and gross segment morphologies are closely linked to magma supply [cf., *Eason et al.*, 2016]. We observed four distinct types of back-arc spreading segments, summarized in Figure 17: (I) *magmatic segments*, characterized by significant axial volcanic rises (~500–550 m) that lack deep valleys and are dominated by smooth volcanic terrain; (II) *magmatic segments currently undergoing tectonic extension*, characterized by an hourglass shape (focused magmatism at a midsegment high), moderate axial valley relief (450–500 m), and abundant smooth volcanic terrain with few hummocky volcanic ridges at the segment centers; (III) *tectonic segments*, characterized by axial valleys with moderate-to-high relief at the segment center (~800–1250 m), low hummocky axial volcanic ridges (~100–450 m) with central grabens, and abundant faulting within the axial valley; and (IV) *tectonic segments currently undergoing magmatic extension*, characterized by axial valleys with moderate-to-high relief at the segment center (600–1300 m), prominent hummocky axial volcanic ridges (~800–1050 m) that lack central grabens, and limited faulting within the axial valley. The southern segments, 12.8°N and 13.3°N, are type I; segments 16.5°N and 17.0°N are type II; segments 13.9°N, 14.5°N, 15.1°N, 16.1°N, and 17.8°N are type III; segments 15.5°N and 18.2°N are type IV (Table 1; Figure 18). Figure 19 shows an along-axis profile along the Mariana back-arc spreading center, highlighting the magmatically-robust versus tectonically-dominated segment types. The diversity of across-axis segment morphologies and seafloor depths is similar to the MAR [e.g., *Devey et al.*, 2010], associated with along-axis variations in crustal thickness related to magma supply. For example, the within-axis high and hourglass-shaped segment morphology of the Turtle Pits area (3°S, MAR [*Devey et al.*, 2010]) is similar to the Type II segment in the Mariana back-arc at 17.0°N.

The volume of neovolcanic material in conjunction with spreading rates determined by *Kato et al.* [2003] can be used as a first-order estimate of the eruption rates and magma supply along each of

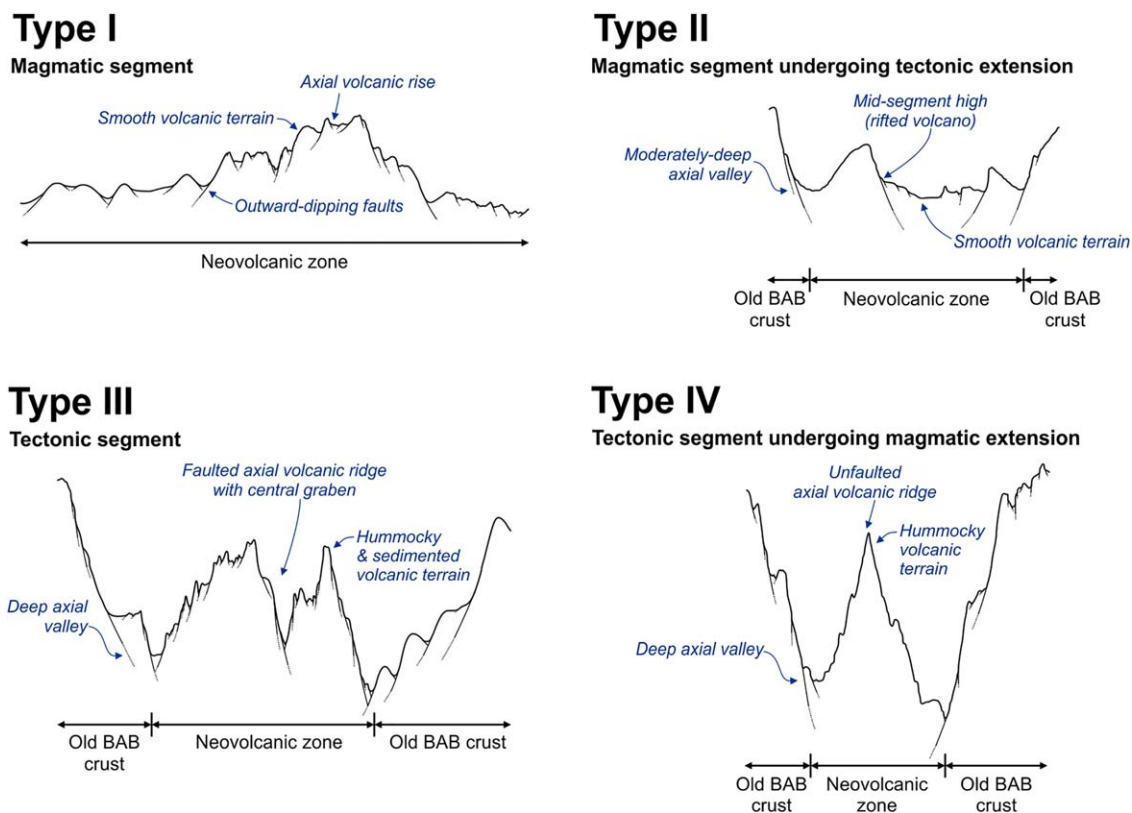


**Figure 17.** Distinguishing cross-sectional features of the back-arc segment types found in the southern and central Mariana back-arc.

the segments studied here (Table 1; supporting information). The eruption rate per kilometer along each segment appears to decrease northward from  $9377 \text{ m}^3 \text{ yr}^{-1} \text{ km}^{-1}$  along the  $13.9^\circ\text{N}$  segment to  $3912 \text{ m}^3 \text{ yr}^{-1} \text{ km}^{-1}$  along the  $15.5^\circ\text{N}$  segment. There is an increase in eruption rates and magma supply along the  $16.1^\circ\text{N}$ ,  $16.5^\circ\text{N}$ , and  $17.0^\circ\text{N}$  segments. The highest eruption rates along the  $17.0^\circ\text{N}$  type II segment ( $31,600 \text{ m}^3 \text{ yr}^{-1} \text{ km}^{-1}$ ), consistent with the abundance of sheet flows at the center of this segment. Estimated eruption rates are highly variable for the tectonic segments (types III and IV), all of which are dominated by hummocky pillow lava flows.

The rate of magma supply on the global mid-ocean ridges is on the order of  $18 \text{ km}^3 \text{ yr}^{-1}$  [Sigurdsson, 2000]. Volcanic arcs account for a much smaller proportion of submarine magmatism, on the order of  $2\text{--}5 \text{ km}^3 \text{ yr}^{-1}$  [Arculus, 1999]. The global MOR average is equivalent to about  $300 \text{ km}^3$  per kilometer of ridge length every 1 million years. By comparison, the estimated eruption rates along the Mariana back-arc are less than  $11 \text{ km}^3$  per kilometer of ridge length over the same time period. Although about 20 or 30 times smaller than on global mid-ocean ridges, the eruption rate at the center of one segment ( $17.0^\circ\text{N}$ ) was large enough to have produced a neovolcanic ridge with a volume comparable to some of the largest shield-type MOR axial volcanoes (e.g.,  $>470 \text{ km}^3$  Axial Volcano on the Juan de Fuca Ridge). Along this segment, additional crustal permeability may be associated with segment-scale shearing produced by the reactivation of the adjacent shear zone [Deschamps *et al.*, 2005].

Local variations in magma supply in the back-arc may be influenced by magmatism associated with cross-arc volcanic chains. These cross-arc chains are associated with either extension or compression in the back-arc as a result of the arcuate geometry of the subduction zone (Figure 18) [Heeszel *et al.*, 2008]. The cross-arc chains at  $16^\circ35'\text{N}$  and  $17^\circ15'\text{N}$  are associated with  $\sim\text{N-S}$  extension in the arc, while the back-arc is undergoing compression. These corridors may provide the structural pathways for focusing magmatic activity, contributing to the development of the large volcanic cone at the southern end of the  $16.5^\circ\text{N}$  segment and increased magmatism at the centers of the  $16.5^\circ\text{N}$  and  $17.0^\circ\text{N}$  segments, as described by Asada *et al.* [2007]. In contrast, the cross-arc volcanic chain at  $14^\circ40'\text{N}$  beginning near



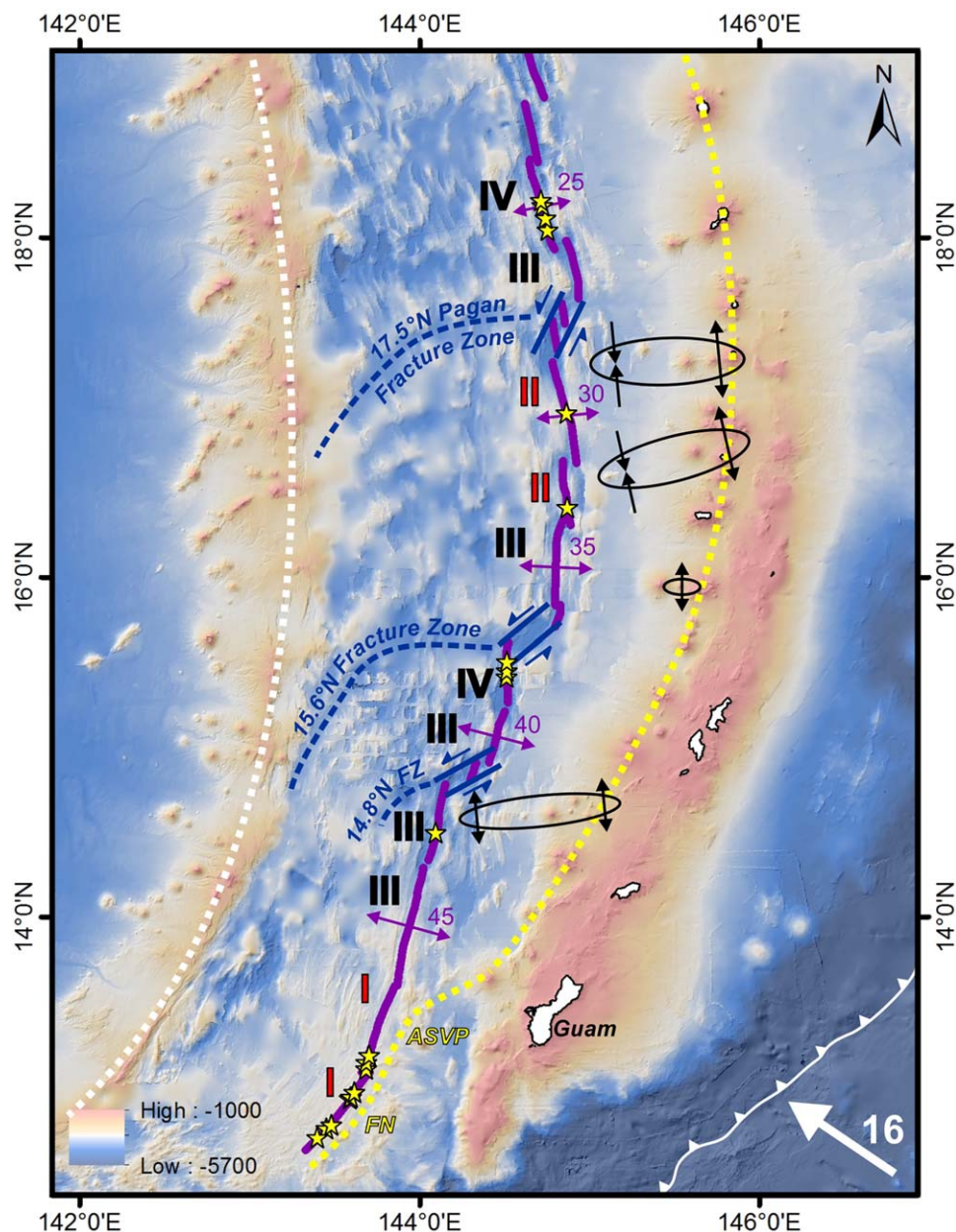


**Figure 18.** Important tectonic features that affect magma supply and segment morphology in the central and southern Mariana back-arc include: (1) oblique subduction; (2) a curved plate margin; (3) arc volcanism near the spreading axis in the south; (4) southward-increasing spreading rates (5) three major shear zone offsets associated with regionally-extensive fracture zones; and (6) ~N-S extension and/or compression along active volcanic cross-chains associated with westward-convex plate curvature. White dotted line = remnant volcanic arc (West Mariana Ridge); yellow dotted line = active volcanic arc; white arrow = convergence direction and rate ( $\text{mm yr}^{-1}$ ) [deMets et al., 2010]; purple line = back-arc spreading axis, with spreading direction (this study) and rate ( $\text{mm yr}^{-1}$ ) [Kato et al., 2003]; blue lines = sinistral shear zone offsets and associated fracture zones; black ellipses = zones of cross-chain extension-compression indicated by seismicity [Heeszel et al., 2008]; red numbers (I, II) = magmatically-robust segments; and black numbers (III, IV) = tectonic segments (see text for segment classification); yellow stars = hydrothermal vent sites [Resing and Shipboard Scientific Party, 2016; Baker et al., 2016]; ASVP = Alphabet Seamount Volcanic Province; FN = Fina Nagu volcanic complex; FZ = fracture zone.

Northwest Rota seamount (Figure 18) is associated with increased seismicity and ~N-S extension in both the arc and back-arc [Heeszel et al., 2008]. The back-arc spreading center at this latitude is heavily faulted and appears to be undergoing mainly tectonic extension, with reduced magma supply and the occurrence of two oceanic core complexes (Figure 7). It appears, therefore, that not all cross-arc structures are necessarily exploited by rising magma.

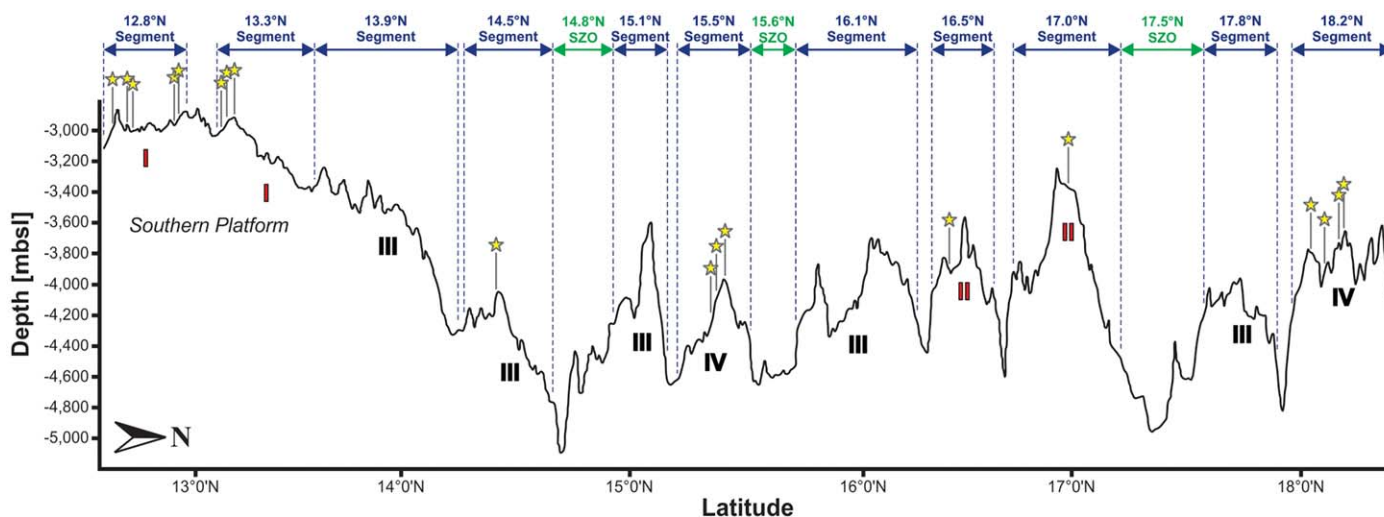


**Figure 19.** An along-axis bathymetric profile from south to north along the Mariana back-arc spreading axis, highlighting the different segment types: red numbers (I, II) indicate magmatically-robust segments, and black numbers (III, IV) indicate tectonically-dominated segments (see text and Figure 17 for detailed descriptions). Yellow stars = hydrothermal vent sites [Resing and Shipboard Scientific Party, 2016; Baker et al., 2016]; SZO = shear zone offset.

#### 7.4 Relationship to Hydrothermal Venting

Eighteen individual hydrothermal vent sites have been identified along seven of the back-arc segments; 12 of which were discovered during the FK151121 expedition (Figure 18) [Resing and Shipboard Scientific Party, 2016; Baker et al., 2016]. Hydrothermal venting was located on every segment type in the Marianas back-arc (Figures 18 and 19). In every case, the venting occurs near the segment centers where magmatic activity is also focused (Figure 19).

Magmatic segments (type I) in the southern back-arc are associated with several hydrothermal vents. The similarity of these “magmatic” segments with fast-spreading ridges suggests the influence of a shallow axial magma chamber that may drive numerous closely-spaced hydrothermal systems [e.g., Hannington, 2009; Hannington et al., 2011; German et al., 2016]. At these high magmatic intensities, the crust behaves ductilely, prohibiting the formation of deeply penetrating faults, thus confining the hydrothermal circulation to the shallow crust [e.g., Devey et al., 2010].

The slower spreading rates of central back-arc segments ( $<40 \text{ mm yr}^{-1}$ ) [Kato et al., 2003] provide more favorable conditions for larger but more widely spaced hydrothermal upflow [Baker and German, 2004; Baker, 2007]. German et al. [2016] noted that hydrothermal activity on slow-spreading ridges may, in fact, be significantly enhanced by the strong tectonic control on fluid flow. Deeply penetrating faults in these settings allow circulation of seawater to considerable depths and, in some cases, at some distance off axis, so that some unusually large hydrothermal systems are found on slow ( $20\text{--}50 \text{ mm yr}^{-1}$ ) and ultraslow-spreading ( $<20 \text{ mm yr}^{-1}$ ) ridges where few were expected at all. All the hydrothermal prospecting along the central Mariana back-arc to date has been confined to the spreading axis.

Type II segments are characterized by focused magmatism with moderate magmatic intensities, resulting in frequent magmatic events that may maintain continuous hydrothermal circulation over long periods of time (e.g., Turtle Pits region on the MAR) [Devey et al., 2010]. The largest mid-segment high occurs at  $17.0^\circ\text{N}$ , where large, vigorously venting chimneys have been observed [Gray, 2016; Butterfield et al., 2017]. However, repeated volcanic eruptions may frequently “pave-over” the hydrothermal vent sites, preventing large accumulations of massive sulfides at the seafloor [e.g., Fouquet, 1997; Anderson et al., 2016].

Tectonic segments (type III) may be associated with increased crustal permeability, which is the primary factor governing the location, intensity, and temperature of hydrothermal circulation [Wilcock, 1998]. One small plume on a type III segment at  $14.5^\circ\text{N}$  is associated with heavy faulting and N-S extension related to cross-arc volcanism, producing the most structurally complex segment in the back-arc. The oceanic core complexes along this segment are important targets for exploration, as some of the world’s largest seafloor massive sulfide deposits have been discovered on core complexes along mid-ocean ridges (e.g., Semenov ore district, MAR,  $13^\circ31'\text{N}$ ) [Pertsev et al., 2012].



Tectonic segments currently undergoing magmatic extension (type IV) were also found to have large plumes along the axial volcanic ridges, associated with observations of both focused and diffuse venting (15.5°N, 18.2°N) [Resing and Shipboard Scientific Party, 2016; Butterfield et al., 2017]. High acoustic backscatter and direct seafloor observations suggest that some of the hydrothermal venting is directly related to recent volcanism [Resing and Shipboard Scientific Party, 2016]. Hydrothermal activity along the 18.2°N segment (including the Central Trough, Burke, Alice Springs and Illium vent sites) has been ongoing for at least 35 years [Craig et al., 1987; Gamo and Shipboard Scientific Party, 1994; Butterfield et al., 2017]. However, along these segments, volcanic events are rare and have a generally low volume, driving only short-lived (i.e., <1200 year) hydrothermal circulation.

Compared to slow-spreading mid-ocean ridges, the Mariana back-arc is associated with additional tectonic complexities (including cross-arc volcanism, oblique extension, and input of arc magmas; Figure 18) that promote increased crustal permeability (e.g., 14.5°N segment) or enhanced magmatism (e.g., 12.8°N and 17.0°N segments), providing favorable sites for the accumulation of large massive sulfide deposits.

## 8. Conclusions

Back-arc spreading centers share a number of features in common with both fast and slow-spreading mid-ocean ridges but have additional tectonic complexities related to oblique convergence, plate rotation, asymmetric extension, and subduction-zone collisions [Hannington et al., 2005]. Within the Mariana back-arc, large-scale structures control the segmentation of the back-arc spreading axis, some potentially related to inherited basement structures marked by distinctive cross-arc volcanic chains. Along the southern and central back-arc spreading center, most of the offset occurs along three major shear zone offsets, which are oblique to the spreading axis as a result of asymmetric extension. In contrast to mid-ocean ridges, which are characterized by transform faults oriented perpendicular to the ridge axis, this can result in large-scale crustal permeability of the type previously described for extensional transform boundaries, for example, in the Eastern Manus Basin [Taylor et al., 1994]. In the Mariana back-arc, this is best illustrated by the re-activation of the shear zone offset at 17.5°N, which has induced oblique spreading in the adjacent segments.

Magmatism in the southern Mariana back-arc is highly influenced by proximity to the volcanic arc, which may contribute melt to the spreading center. Where magma supply rates are enhanced by melt from the arc, ridge morphologies resemble fast-spreading mid-ocean ridges. Farther away from the arc, the central Mariana spreading centers strongly resemble slow-spreading mid-ocean ridges, with deep axial valleys containing axial volcanic ridges, strong magma focusing at mid-segment highs, large-scale detachment faulting, and ridge segmentation dominated by second and third-order discontinuities (OSCs and DEVALS). Melts may be focused into the spreading segments where long-lived cross-arc structures are present. Four different segment types are recognized: magmatic segments (type I), magmatic segments currently undergoing tectonic extension (Type II), tectonic segments (type III), and tectonic segments currently undergoing magmatic extension (Type IV). Type I segments occur in the southern back-arc and—despite the slow-spreading rate—closely resemble fast-spreading mid-ocean ridges with high-level magmatism and shallow-crustal hydrothermal circulation. The gradual change in segment morphology with proximity to the volcanic arc supports earlier suggestions of a strong influence by melt contributions from the arc. Tectonically influenced segments (type II, III, and IV) occur in the central Mariana back-arc, and bear a closer resemblance to slow-spreading mid-ocean ridges in terms of ridge morphology, structure, magma supply rates, and hydrothermal activity. North-south extension occurs along cross-arc structures near the arc front [Heeszel et al., 2008]. One such structure extends into the back-arc near the 14.5°N segment, which is characterized by abundant faulting and the development of oceanic core complexes. Further from the volcanic arc toward the back-arc, cross-chains are associated with N-S compression and focused magmatism along the 16.5°N and 17.0°N segments. This focused magmatism produces the characteristic hourglass segment morphology, where the axial valley is dominated by smooth sheet flows along central axial volcanic highs, in sharp contrast to the hummocky pillow mounds and ridges that occur throughout most of the central back-arc.

Hydrothermal activity in the Mariana back-arc is broadly similar to that on mid-ocean ridges, and is localized where a heat source is present to drive hydrothermal circulation, and faulting focuses fluid flow. Recent discoveries along the spreading axis of every segment type indicate a primary magmatic control on venting.

By comparison with slow-spreading ridges [e.g., *Devey et al.*, 2010; *German et al.*, 2016], the greatest potential for large massive sulfide accumulations is in the type II segment at 17.0°N and the type III segment at 14.5°N. As hydrothermal outflow is strongly influenced by crustal permeability, our mapping of the fault patterns provides a means to examine the relationships between large-scale tectonic processes (and associated volcanism) with hydrothermal venting as discoveries continue to be made.

### Acknowledgments

We would like to thank the Schmidt Ocean Institute and the captain and crew of the *R/V Falkor* (FK151121). We gratefully acknowledge the at-sea support by the AUV *Sentry* team. We would also like to thank the science teams of the EX1605L1–2 “Deep Water Exploration of the Marianas” cruises, as well as the ROV *Deep Discoverer* team and captain and crew of the *Okeanos Explorer*. Funding for this project was provided by the NOAA Ocean Exploration and Research Program (NOAA-OER-2016–003) and the NOAA Pacific Islands Regional Office. This publication is partially funded by the Joint Institute for the Study of the Atmosphere and Ocean (JISAO) under NOAA Cooperative Agreement NA10OAR4320148 (2010–2015) and NA15OAR4320063 (2015–2020), contribution 2017–066, and by the NOAA/PMEL Earth-Ocean Interactions Program, contribution 4621. Additional support was awarded to MOA through an NSERC Alexander Graham Bell Canadian Graduate Scholarship (CGS-D) and Michael Smith Foreign Study Supplement, an SEG Canada Foundation Research Grant, and the Schmidt Ocean Institute Student Opportunities Program, and an NSERC Discovery Grant to MDH. Additional data is available in the electronic Supplementary Information associated with this publication. Bathymetric data collected during the *R/V Falkor* cruise (FK151121) can be found at <http://www.rvdata.us/catalog/FK151121>, and bathymetric data collected during the *R/V Okeanos Explorer* cruise (EX1605L1–2) can be found at <http://oceanexplorer.noaa.gov/okeanos/collaboration-tools/ftp/welcome.html>. This manuscript was greatly improved by the thoughtful reviews provided by an anonymous reviewer.

### References

- Ambos, E. L., and D. M. Hussong (1982), Crustal Structure of the Mariana Trough, *J. Geophys. Res.*, *87*(B5), 4003–4018, doi:10.1029/JB087iB05p04003.
- Anderson, M. O., M. D. Hannington, K. Haase, U. Schwarz-Schampera, N. Augustin, T. F. McConachy, and K. Allen (2016), Tectonic focusing of voluminous basaltic eruptions in magma-deficient backarc rifts, *Earth Planet. Sci. Lett.*, *440*, 43–55, doi:10.1016/j.epsl.2016.02.002.
- Arculus, R. J. (1999), Origins of the continental crust, *J. Proc. R. Soc. N. S. W.*, *132*, 83–110.
- Asada, M., A. Deschamps, T. Fujiwara, and Y. Nakamura (2007), Submarine lava flow emplacement and faulting in the axial valley of two morphologically distinct spreading segments of the Mariana back-arc basin from Wadatsumi side-scan sonar images, *Geochem. Geophys. Geosyst.*, *8*, Q04001, doi:10.1029/2006GC001418.
- Augustin, N., F. M. van der Zwan, C. W. Devey, M. Ligi, T. Kwasnitschka, P. Faldens, R. A. Bantan, and A. S. Basaham (2016), Geomorphology of the central Red Sea Rift: Determining spreading processes, *Geomorphology*, *274*, 162–179, doi:10.1016/j.geomorph.2016.08.028.
- Baker, E. T. (2007), Hydrothermal cooling of mid-ocean ridge axes: Do measured and modeled heat fluxes agree?, *Earth Planet. Sci. Lett.*, *263*(1–2), 140–150, doi:10.1016/j.epsl.2007.09.010.
- Baker, E. T., and C. R. German (2004), On the global distribution of hydrothermal vent fields, in *Mid-Ocean Ridges: Hydrothermal Interactions Between the Lithosphere and Oceans*, edited by C. R. German, J. Lin, and M. Parson, pp. 245–266, AGU, Washington, D. C.
- Baker, E. T., G. J. Massoth, K. Nakamura, R. W. Embley, C. E. J. De Ronde, and R. J. Arculus (2005), Hydrothermal activity on near-arc sections of back-arc ridges: Results from the Mariana Trough and Lau Basin, *Geochem. Geophys. Geosyst.*, *6*, Q09001, doi:10.1029/2005GC000948.
- Baker, E. T., W. W. J. Chadwick, S. L. Walker, S. G. Merle, J. A. Resing, and M. O. Anderson (2016), Hydrothermal plume surveys of the Mariana Backarc (12.7°–18.3°N) by surface-ship and AUV find an unexpectedly high spatial frequency of vent sites, in *2016 Fall Meeting*, AGU, San Francisco, Calif.
- Baker, N., P. Fryer, F. Martinez, and T. Yamazaki (1996), Rifting history of the northern Mariana Trough: SeaMARC II and seismic reflection surveys, *J. Geophys. Res.*, *101*(B5), 11,427–11,455.
- Becker, N. C., P. F. Fryer, and G. F. Moore (2010), Malaguana-Gadao Ridge: Identification and implications of a magma chamber reflector in the southern Mariana Trough, *Geochem. Geophys. Geosyst.*, *11*, Q04X13, doi:10.1029/2009GC002719.
- Bibee, L. D., G. G. Shor, and R. S. Lu (1980), Inter-arc spreading in the Mariana Trough, *Mar. Geol.*, *35*(1–3), 183–197, doi:10.1016/0025-3227(80)90030-4.
- Bouysson, P., et al. (2010), Geological Map of the World at 1:25 M, 3rd ed., 2 sheets, CGMW, UNESCO, Paris.
- Bracey, D. R., and T. A. Ogden (1972), Southern Mariana Arc: Geophysical observations and hypothesis of evolution, *Bull. Geol. Soc. Am.*, *83*, 1509–1522, doi:10.1130/0016-7606(1972)83[1509:SMAGOA]2.0.CO;2.
- Brounce, M., K. A. Kelley, R. Stern, F. Martinez, and E. Cottrell (2016), The Fina Nagu volcanic complex: Unusual submarine arc volcanism in the rapidly deforming southern Mariana margin, *Geochem. Geophys. Geosyst.*, *17*, 4078–4091, doi:10.1002/2016GC006457.
- Brown, L. (2010), A new technique for depicting terrain relief, in *NACIS Annual Meeting*, pp. 1–14, North American Cartographic Information Society (NACIS), St. Petersburg, Florida.
- Buck, W. R., L. L. Lavier, and A. N. B. Poliakov (2005), Modes of faulting at mid-ocean ridges, *Nature*, *434*(7034), 719–723, doi:10.1038/nature03358.
- Butterfield, D., and Shipboard Scientific Party (2017), Hydrothermal hunt at the Mariana back-arc, Leg 2, in *Cruise Report for FK161129 on RV Falkor*, Seattle, Wash., doi:10.7284/907181.
- Campbell, A. C., J. M. Edmond, D. Colodner, M. R. Palmer, and K. K. Falkner (1987), Chemistry of hydrothermal fluids from the Mariana Trough backarc basin in comparison to mid-ocean ridge fluids, in *EOS Trans. AGU*, *68*(44), pp. 1531, AGU, San Francisco, Calif.
- Carlson, R. L., and C. A. Mortera-Gutiérrez (1990), Subduction hinge migration along The Izu-Bonin-Mariana arc, *Tectonophysics*, *181*(1–4), 331–344, doi:10.1016/0040-1951(90)90026-5.
- Craig, H., Y. Horibe, and K. A. Farley (1987), Hydrothermal vents in the Mariana Trough: Results of the first Alvin dives, in *EOS Trans. AGU*, vol. 68, pp. 1531, AGU, San Francisco, Calif.
- DeMets, C., R. G. Gordon, D. F. Argus, and S. Stein (1994), Effect of recent revisions to the geomagnetic reversal time scale on estimate of current plate motions, *Geophys. Res. Lett.*, *21*(20), 2191–2194, doi:10.1029/94GL02118.
- DeMets, C., R. G. Gordon, and D. F. Argus (2010), Geologically current plate motions, *Geophys. J. Int.*, *181*, 1–80, doi:10.1111/j.1365-246X.2009.04491.x.
- Deschamps, A., and T. Fujiwara (2003), Asymmetric accretion along the slow-spreading Mariana Ridge, *Geochem. Geophys. Geosyst.*, *4*(10), 8622, doi:10.1029/2003GC000537.
- Deschamps, A., and S. Lallemand (2002), The West Philippine Basin: An Eocene to early Oligocene back arc basin opened between two opposed subduction zones, *J. Geophys. Res.*, *107*(B12), 2322, doi:10.1029/2001JB001706.
- Deschamps, A., T. Fujiwara, M. Asada, P. Gente, Y. Nakamura, A. Heuret, K. Naito, H. Horikawa, and S. Saganuma (2004), Deep-tow sonar survey of the Mariana spreading axis: Initial results of the KR03–12 cruise, *InterRidge News*, *13*, 6–9.
- Deschamps, A., T. Fujiwara, M. Asada, L. Montési, and P. Gente (2005), Faulting and volcanism in the axial valley of the slow-spreading center of the Mariana back arc basin from Wadatsumi side-scan sonar images, *Geochem. Geophys. Geosyst.*, *6*, Q05006, doi:10.1029/2004GC000881.
- Devey, C. W., C. R. German, K. M. Haase, K. S. Lackschewitz, B. Melchert, and D. P. Connelly (2010), The relationships between volcanism, tectonism and hydrothermal activity on the Mid-Atlantic Ridge south of the equator, in *Diversity of Hydrothermal Systems on Slow Spreading Ocean Ridges*, vol. 188, edited by P. A. Rona et al., pp. 133–152, AGU, Washington, D. C.
- Dixon, T. H., and R. J. Stern (1983), Petrology, chemistry, and isotopic composition of submarine volcanoes in the southern Mariana arc., *Geol. Soc. Am. Bull.*, *94*, 1159–1172, doi:10.1130/0016-7606(1983)94 <1159:PCAICO>2.0.CO;2.
- Eason, D. E., R. A. Dunn, J. P. Canales, and R. Sohn (2016), Segment-scale variations in seafloor volcanic and tectonic processes from multi-beam sonar imaging, mid-Atlantic Ridge Rainbow region (35°45′–36°35′N), *Geochem. Geophys. Geosyst.*, *17*, 3560–3579, doi:10.1002/2016GC006433.



- Einarsson, P., and J. Eiríksson (1982), Earthquake fractures in the Districts Land and Rangárvellir in the South Iceland Seismic Zone, *Jökull*, 32, 113–120.
- Engdahl, R. E., R. van der Hilst, and R. Buland (1998), Global teleseismic earthquake relocation with improved travel times and procedures for depth determination, *Bull. Seismol. Soc. Am.*, 88(3), 722–743, doi:10.1130/0-8137-2349-3.461.
- Fouquet, Y. (1997), Where are the large hydrothermal sulphide deposits in the oceans?, in *Philosophical Transactions: Mathematical, Physical and Engineering Sciences*, edited by J. R. Cann, H. Elderfield, A. Laughton, vol. 355, pp. 427–441, The Royal Society A, London, doi: 10.1098/rsta.1997.0015.
- Fryer, P. (1981), Petrogenesis of basaltic rocks from the Mariana Trough, doctoral dissertation, pp. 157, Univ. of Hawai'i, Honolulu, Hawai'i.
- Fryer, P. (1995), Geology of the Mariana Trough, in *Backarc Basins: Tectonics and Magmatism*, edited by B. Taylor, pp. 237–279, Springer, New York, doi:10.1007/978-1-4615-1843-3.
- Fryer, P., and D. M. Hussong (1981), Seafloor spreading in the Mariana Trough: Results of leg 60 drill site selection surveys, *Initial Rep. Deep Sea Drill. Proj.*, 60, 45–55, doi:10.2973/dsdp.proc.60.103.1982.
- Fryer, P., and D. M. Hussong (1982), Arc volcanism in the Mariana Trough, in *EOS Trans. AGU*, 63(45), pp. 1135, AGU, San Francisco, Calif.
- Fryer, P., H. Fujimoto, M. Sekine, L. E. Johnson, J. Kasahara, H. Masuda, T. Gamo, T. Ishii, M. Ariyoshi, and K. Fujioka (1998), Volcanoes of the southwestern extension of the active Mariana Island arc: New swath-mapping and geochemical studies, *Isl. Arc*, 7(3), 596–607, doi: 10.1111/j.1440-1738.1998.00212.x.
- Fryer, P., N. Becker, B. Appelgate, F. Martinez, M. Edwards, and G. Fryer (2003), Why is the Challenger Deep so deep?, *Earth Planet. Sci. Lett.*, 211(3–4), 259–269, doi:10.1016/S0012-821X(03)00202-4.
- Fujikura, K., T. Yamazaki, K. Hasegawa, U. Tsunogai, R. J. Stern, H. Ueno, H. Yamamoto, C. -H. Sun, and T. Okutani (1997), Biology and earth scientific investigation by the submersible “Shinkai 6500” system of deep-sea hydrothermalism and lithosphere in the Mariana back-arc basin, *JAMSTEC J. Deep Sea Res.*, 13, 1–20.
- Fujiwara, T., S. Umino, M. Asada, Y. Koike, K. Kimoto, T. Kanamatsu, and S. Okada (2008), A submersible study of the Mariana Trough back-arc spreading center at 17°N, *JAMSTEC J. Deep Sea Res.*, 8, 61–73, doi:10.5918/jamstecr.8.61.
- Gamo, T., and Shipboard Scientific Party (1993), Revisits to the mid-Mariana Trough hydrothermal site and discovery of new venting in the southern Mariana region by the Japanese submersible Shinkai 6500, *InterRidge News*, 2, 11–14.
- Gamo, T., and Shipboard Scientific Party (1994), Mariana 1992 diving surveys by “Shinkai 6500” (Y9204 cruise): Revisits to the Mid-Mariana hydrothermal area and discovery of hydrothermal vents in the southern Mariana region, *JAMSTEC J. Deep Sea Res.*, 10, 153–162.
- German, C. R., S. Petersen, and M. D. Hannington (2016), Hydrothermal exploration of mid-ocean ridges: Where might the largest sulfide deposits be forming?, *Chem. Geol.*, 420, 114–126, doi:10.1016/j.chemgeo.2015.11.006.
- Gray, L. M. (2016), Mapping data acquisition and processing summary report, in *Cruise EX-16-05 Leg 1: 2016 Deepwater Exploration of the Marianas*, pp. 1–19, NOAA Off. of Ocean Explor. and Res., Silver Spring, Md.
- Gribble, R. F., R. J. Stern, S. H. Bloomer, D. Stüben, T. O'Hearn, and S. Newman (1996), MORB mantle and subduction components interact to generate basalts in the southern Mariana Trough back-arc basin, *Geochim. Cosmochim. Acta*, 60, 2153–2166, doi:10.1016/0016-7037(96)00078-6.
- Gribble, R. F., R. J. Stern, S. Newman, S. H. Bloomer, and T. O'Hearn (1998), Chemical and isotopic composition of lavas from the Northern Mariana Trough: Implications for magmagenesis in back-arc basins, *J. Petrol.*, 39, 125–154, doi:10.1093/ptro/39.1.125.
- Grindlay, N. R., P. J. Fox, and K. C. Macdonald (1991), 2nd-order ridge axis discontinuities in the South-Atlantic: Morphology, structure, and evolution, *Mar. Geophys. Res.*, 13(1), 21–49.
- Gvirtzman, Z., and R. J. Stern (2004), Bathymetry of Mariana trench-arc system and formation of the Challenger Deep as a consequence of weak plate coupling, *Tectonics*, 23, TC2011, doi:10.1029/2003TC001581.
- Hall, R., J. R. Ali, C. D. Anderson, and S. J. Baker (1995), Origin and motion history of the Philippine Sea Plate, *Tectonophysics*, 251, 229–250, doi:10.1016/0040-1951(95)00038-0.
- Hannington, M., J. Jamieson, T. Monecke, S. Petersen, and S. Beaulieu (2011), The abundance of seafloor massive sulfide deposits, *Geology*, 39(12), 1155–1158, doi:10.1130/G32468.1.
- Hannington, M. D. (2009), Modern submarine hydrothermal systems: A global perspective on distribution, size, and tectonic setting, in *Submarine Volcanism and Mineralization: Modern Through Ancient, Short Course Notes*, vol. 19, edited by B. Cousens and S. J. Piercey, pp. 91–148, Geol. Assoc. of Can. Miner. Deposits Div., St. John's, N. L.
- Hannington, M. D., C. E. J. de Ronde, and S. Petersen (2005), Sea-floor tectonics and submarine hydrothermal systems, *Econ. Geol.*, 100, 111–141.
- Hawkins, J. W., P. F. Lonsdale, J. D. Macdougall, and A. M. Volpe (1990), Petrology of the axial ridge of the Mariana Trough backarc spreading center, *Earth Planet. Sci. Lett.*, 100, 226–250, doi:10.1016/0012-821X(90)90187-3.
- Heessel, D. S., D. A. Wiens, P. J. Shore, H. Shiohara, and H. Sugioka (2008), Earthquake evidence for along-arc extension in the Mariana Islands, *Geochem. Geophys. Geosyst.*, 9, Q12X03, doi:10.1029/2008GC002186.
- Hessler, R. R., and P. F. Lonsdale (1991), Biogeography of Mariana Trough hydrothermal vent communities, *Deep Sea Res. Part A*, 38(2), 185–199, doi:10.1016/0198-0149(91)90079-U.
- Hessler, R. R., and J. W. Martin (1989), *Austinograea williamsi*, New Genus, New Species, a hydrothermal vent crab (Decapoda: Bythograeidae) from the Mariana Back-Arc basin, western Pacific, *J. Crustacean Biol.*, 9(4), 645–661, doi:10.2307/1548594.
- Hessler, R. R., P. Lonsdale, and J. Hawkins (1988), Patterns on the ocean floor, *New Sci.*, 24, 47–51.
- Hewitt, A., R. Salisbury, and J. Wilson (2010), Using multibeam echosounder backscatter to characterize seafloor features, *Sea Technol.*, 51(9), 10–13, doi:10.4043/20672-MS.
- Hilde, T. W. C., and C.-S. Lee (1984), Origin and evolution of the West Philippine Basin: A new interpretation, *Tectonophysics* 102, 85–104.
- Hsui, A. T., and S. Youngquist (1985), A dynamic model of the curvature of the Mariana Trench, *Nature*, 318(5), 455–457, doi:10.1038/314731a0.
- Hussong, D. M., and S. Uyeda (1981), Tectonic processes and the history of the Mariana Arc: A synthesis of the results of Deep Sea Drilling Project Leg 60, *Initial Rep. Deep. Drill. Proj.*, 60, 909–929, doi:10.2973/dsdp.proc.60.154.1982.
- Ikehata, K., R. Suzuki, S. Sazuhiko, J. Ishibashi, and T. Urabe (2015), Mineralogical and geochemical characteristics of hydrothermal minerals collected from hydrothermal vent fields in the southern Mariana spreading center, in *Subseafloor Biosphere Linked to Hydrothermal Systems: TAIGA Concept*, edited by J. Ishibashi, K. Okino, and M. Sunamura, pp. 275–287, Springer, Japan.
- Ishibashi, J., T. Yamanaka, H. Kimura, A. Hirota, T. Toki, U. Tsunogai, T. Gamo, M. Utsumi, K. Roe, S. Miyabe, and K. Okamura (2004), Geochemistry of hydrothermal fluids in south Mariana backarc spreading center, in *Eos Trans. AGU*, 85(47), Fall Meet. Suppl., Abstract V44A-05.
- Ishibashi, J. -I., U. Tsunogai, T. Toki, N. Ebina, T. Gamo, Y. Sano, H. Masuda, and H. Chiba (2015), Chemical composition of hydrothermal fluids in the central and southern Mariana Trough backarc basin, *Deep. Sea Res., Part II*, 121, 126–136, doi:10.1016/j.dsr2.2015.06.003.

- Jarrard, R. D. (1986), Relations among subduction parameters, *Rev. Geophys.*, 24(2), 217–284, doi:10.1029/RG024i002p00217.
- Jenner, G. A., P. A. Cawood, M. Rautenschlein, and W. M. White (1987), Composition of back-arc basin volcanics, Valu Fa Ridge, Lau Basin: Evidence for a slab-derived component in their mantle source, *J. Volcanol. Geotherm. Res.*, 32(1–3), 209–222, doi:10.1016/0377-0273(87)90045-X.
- Johnson, L. E., P. Fryer, H. Masuda, T. Ishii, and T. Gamo (1993), Hydrothermal vent deposits and two magma sources for volcanoes near 13°20'N in the Mariana backarc basin: A view from Shinkai 6500, in *EOS Trans. AGU*, 74(43), pp. 681, AGU, San Francisco, USA.
- Takegawa, T., M. Utsumi, and K. Marumo (2008), Geochemistry of sulfide chimneys and basement pillow lavas at the southern Mariana Trough (12.55°N–12.58°N), *Resour. Geol.*, 58(3), 249–266, doi:10.1111/j.1751-3928.2008.00060.x.
- Karig, D. E. (1971a), Origin and development of marginal basins in the western Pacific, *J. Geophys. Res.*, 76(11), 2542–2561, doi:10.1007/s11192-012-0776-8.
- Karig, D. E. (1971b), Structural history of the Marianas island arc system, *Geol. Soc. Am. Bull.*, 82, 323–344, doi:10.1130/0016-7606(1971)82[323:SHOTMI]2.0.CO;2.
- Karig, D. E., R. N. Anderson, and L. D. T. Bibee (1978), Characteristics of back arc spreading in the Mariana Trough, *J. Geophys. Res.*, 83(B3), 1213–1226, doi:10.1029/JB083iB03p01213.
- Kato, T., J. Beavan, T. Matsushima, Y. Kotake, J. T. Camacho, and S. Nako (2003), Geodetic evidence of back-arc spreading in the Mariana Trough, *Geophys. Res. Lett.*, 30(12), 1625, doi:10.1029/2002GL016757.
- Kennelly, P. J. (2008), Terrain maps displaying hill-shading with curvature, *Geomorphology*, 102(3–4), 567–577, doi:10.1016/j.geomorph.2008.05.046.
- Kennelly, P. J., and A. J. Stewart (2014), General sky models for illuminating terrains, *Int. J. Geogr. Inf. Sci.*, 28(2), 383–406, doi:10.1080/13658816.2013.848985.
- Kong, L. S. L. (1993), Seafloor spreading in the Mariana Trough, in *Preliminary Report of the Hakuu-Maru Cruise KH92-1*, edited by J. Segawa, pp. 5–16, Ocean Res. Inst., Univ. Tokyo, Tokyo.
- Kong, L. S. L., N. Seama, H. Fujimoto, J. Kasahara, and KH92-1 Shipboard Scientific Party (1992), Segmentation of the Mariana Trough back-arc spreading center at 18°N, *InterRidge News*, 1(1), 2–5.
- Koyama, M., S. Cisowski, and P. Pezard (1992), Paleomagnetic evidence for northward drift and clockwise rotation of the Izu-Bonin forearc since the early Oligocene, in *Proceedings of the Ocean Drilling Program, Scientific Results*, vol. 126, edited by B. Taylor et al., pp. 353–370, Ocean Drill. Program, College Station, Tex.
- LaTraille, S., and D. Hussong (1980), Crustal structure across the Mariana island arc, in *The Tectonic and Geologic Evolution of Southeast Asian Seas and Islands*, edited by D. Hayes, pp. 209–221, AGU, Washington, D. C.
- Le Pichon, X., and P. H. Huchon (1987), Central Japan triple junction revisited, *Tectonics*, 6(1), 35–45, doi:10.1029/TC006i001p00035.
- Le Pichon, X., P. H. Huchon, and E. Barrier (1985), Pangea, geoid and the evolution of the western margin of the Pacific Ocean, in *Formation of Active Ocean Margins*, edited by N. Nasu et al., pp. 3–42, Terra-pub, Tokyo.
- Lobecker, E. (2016), *Oceanographic Data Collected During the EX1605L2 (CAPSTONE CNMI & Mariana Trench MNM (Mapping)) on NOAA Ship OKEANOS EXPLORER in the North Pacific Ocean From 2016-05-20 to 2016-06-11 (NCEI Accession 0155917)*, version 1.1 [data set], NOAA Natl. Cent. for Environ. Inform., doi:10.7289/V5Z03663.
- Macdonald, K. C. (1982), Mid-ocean ridges: Fine scale tectonic, volcanic and hydrothermal processes within the plate boundary zone, *Annu. Rev. Earth Planet. Sci.*, 10, 155–190, doi:10.1146/annurev.ea.10.050182.001103.
- Macdonald, K. C. (2001), Mid-ocean ridge tectonics, volcanism, and geomorphology, *Encycl. Ocean Sci.*, 3, 1798–1813, doi:10.1016/B978-012374473-9.00094-1.
- MacLeod, C. J., R. C. Searle, B. J. Murton, J. F. Casey, C. Mallows, S. C. Unsworth, K. L. Achenbach, and M. Harris (2009), Life cycle of oceanic core complexes, *Earth Planet. Sci. Lett.*, 287(3–4), 333–344, doi:10.1016/j.epsl.2009.08.016.
- Martínez, F., P. Fryer, N. A. Baker, and T. Yamazaki (1995), Evolution of backarc rifting: Mariana Trough, 20°–24°N, *J. Geophys. Res.*, 100(B3), 3807–3827, doi:10.1029/94JB02466.
- Martínez, F., P. Fryer, and N. Becker (2000), Geophysical characteristics of the southern Mariana Trough, 11°50'N–13°40'N, *J. Geophys. Res.*, 105(B7), 16,591–16,607, doi:10.1029/2000JB900117.
- Mason, W. G., L. Moresi, P. G. Betts, and M. S. Miller (2010), Three-dimensional numerical models of the influence of a buoyant oceanic plateau on subduction zones, *Tectonophysics*, 483(1–2), 71–79, doi:10.1016/j.tecto.2009.08.021.
- Masuda, H., R. A. Lutz, A. Matsumoto, S. Masumoto, and K. Fujioka (1994), Topography and geochemical aspects on the most recent volcanism around the spreading axis of the southern Mariana Trough at 13°N, *JAMSTEC J. Deep Sea Res.*, 10, 176–185.
- Masuda, H., K. Mitsuzawa, N. Seama, S. Masumoto, and YK-99-11 Shipboard Scientific Party (2001), Bathymetry and hydrothermal activities in the southern Mariana Trough: Reconnaissance results of YK-99-11, *JAMSTEC J. Deep Sea Res.*, 18, 83–88.
- Matthews, K. J., R. D. Miller, P. Wessel, and J. M. Whittaker (2011), The tectonic fabric of the ocean basins, *J. Geophys. Res.*, 116, B12109, doi:10.1029/2011JB008413.
- Maus, S., et al. (2009), EMAG2: A 2-arc min resolution Earth Magnetic Anomaly Grid compiled from satellite, airborne, and marine magnetic measurements, *Geochem. Geophys. Geosyst.*, 10, Q08005, doi:10.1029/2009GC002471.
- McCabe, R., and S. Uyeda (1983), Hypothetical model for the bending of the Mariana Arc, in *The Tectonic and Geologic Evolution of Southeast Asian Seas and Islands: Part 2*, edited by D. E. Hayes, pp. 281–293, AGU, Washington, D. C.
- Miller, M. S., B. L. N. Kennett, and G. S. Lister (2004), Imaging changes in morphology, geometry, and physical properties of the subducting Pacific plate along the Izu-Bonin-Mariana arc, *Earth Planet. Sci. Lett.*, 224, 363–370, doi:10.1016/j.epsl.2004.05.018.
- Miller, M. S., A. Gorbato, and B. L. N. Kennett (2005), Heterogeneity within the subducting Pacific slab beneath the Izu-Bonin-Mariana arc: Evidence from tomography using 3D ray tracing inversion techniques, *Earth Planet. Sci. Lett.*, 235(1–2), 331–342, doi:10.1016/j.epsl.2005.04.007.
- Miller, M. S., A. Gorbato, and B. L. N. Kennett (2006), Three-dimensional visualization of a near-vertical slab tear beneath the southern Mariana arc, *Geochem. Geophys. Geosyst.*, 7, Q06012, doi:10.1029/2005GC001110.
- Mitsuzawa, K., H. Masuda, N. Seama, Y. Hasegawa, M. Miyamoto, N. Togashi, A. So, and H. Yamanobe (2000), Preliminary report of Deep-Tow/Yokosuka Cruise at hydrothermal areas in the mid and southern Mariana, *JAMSTEC J. Deep Sea Res.*, 17, 73–87.
- Müller, R. D., W. R. Roest, J. Y. Royer, L. M. Gahagan, and J. G. Sclater (1997), Digital isochrons of the world's ocean floor, *J. Geophys. Res.*, 102(B2), 3211–3214, doi:10.1029/96JB01781.
- Nakamura, K., T. Toki, N. Mochizuki, M. Asada, J. I. Ishibashi, Y. Nogi, S. Yoshikawa, J. I. Miyazaki, and K. Okino (2013), Discovery of a new hydrothermal vent based on an underwater, high-resolution geophysical survey, *Deep Sea Res., Part 1*, 74, 1–10, doi:10.1016/j.dsr.2012.12.003.
- Oakley, A. J., B. Taylor, G. F. Moore, and A. Goodliffe (2009), Sedimentary, volcanic, and tectonic processes of the central Mariana Arc: Mariana Trough back-arc basin formation and the West Mariana Ridge, *Geochem. Geophys. Geosyst.*, 10, Q08X07, doi:10.1029/2008GC002312.



- Ohara, Y., T. Yoshida, Y. Kato, and S. Kasuga (2001), Giant megamullion in the Parece Vela backarc basin, *Mar. Geophys. Res.*, *22*, 47–61, doi:10.1023/A:1004818225642.
- Okino, K., S. Kasuga, and Y. Ohara (1998), A new scenario of the Parece Vela Basin genesis, *Mar. Geophys. Res.*, *20*(1), 21–40, doi:10.1023/A:1004377422118.
- Pertsev, A. N., N. S. Bortnikov, E. A. Vlasov, V. E. Beltenev, I. G. Dobretsova, and O. A. Ageeva (2012), Recent massive sulfide deposits of the Semenov ore district, Mid-Atlantic Ridge, 13°31' N: Associated rocks of the oceanic core complex and their hydrothermal alteration, *Geol. Ore Depos.*, *54*(5), 334–346, doi:10.1134/S1075701512050030.
- Resing, J. A., and Shipboard Scientific Party (2016), Hydrothermal hunt at Mariana back-arc, in *Cruise Report for FK151121 on RV Falkor*, pp. 107, Seattle, Wash., doi:10.7284/906519.
- Ryan, W. B. F., et al. (2009), Global multi-resolution topography synthesis, *Geochem. Geophys. Geosyst.*, *10*, Q03014, doi:10.1029/2008GC002332.
- Sandwell, D. T., R. D. Müller, W. H. F. Smith, E. Garcia, and R. Francis (2014), New global marine gravity model from CryoSat-2 and Jason-1 reveals buried tectonic structure., *Science*, *346*(6205), 65–7, doi:10.1126/science.1258213.
- Scholz, C. H., and C. Small (1997), The effect of seamount subduction on seismic coupling, *Geology*, *25*(6), 487–490, doi:10.1130/0091-7613(1997)025<0487:TEOSSO>2.3.CO;2.
- Schouten, H., K. D. Klitgord, and J. A. Whitehead (1985), Segmentation of mid-ocean ridges, *Nature*, *317*, 225–229, doi:10.1038/317225a0.
- Scott, R. B., L. Kroenke, G. Zakariadze, and A. Sharaskin (1981), Evolution of the South Philippine Sea: Deep Sea Drilling Project Leg 59 results, in *Initial Report of the Deep Sea Drilling Project 59*, edited by S. Orlofsky, pp. 909–929, U.S. Gov. Print. Off., Washington, D. C.
- Sdrolias, M., W. R. Roest, and R. D. Müller (2004), An expression of Philippine Sea plate rotation: The Parece Vela and Shikoku Basins, *Tectonophysics*, *394*(1–2), 69–86, doi:10.1016/j.tecto.2004.07.061.
- Seama, N., and T. Fujiwara (1993), Geomagnetic anomalies in the Mariana Trough 18°N, in *Preliminary Reports of the Hakuho-Maru Cruise KH92-1*, edited by J. Segawa, pp. 70–71, Ocean Res. Inst., Univ. Tokyo, Tokyo.
- Seno, T. (1985), Age of subducting lithosphere and back-arc basin formation in the Western Pacific since the middle Tertiary, in *Formation of Active Ocean Margins*, edited by N. Nasu et al., pp.469–481, Terra Sci., Tokyo.
- Seno, T., and S. Maruyama (1984), Paleogeographic reconstruction and origin of the Philippine Sea, *Tectonophysics*, *102*, 53–84, doi:10.1016/0040-1951(84)90008-8.
- Severinghaus, J. P., and K. C. Macdonald (1988), High inside corners at ridge-transform intersections, *Mar. Geophys. Res.*, *9*, 353–367, doi:10.1007/BF00315005.
- Sigmundsson, F. (2006), *Iceland Geodynamics: Crustal Deformation and Divergent Plate Tectonics*, Springer, Chichester, U. K.
- Sigurdsson, H. (2000), Volcanic episodes and rates of volcanism, in *Encyclopedia of Volcanoes*, edited by H. Sigurdsson et al., pp. 271–279, Academic, San Diego, Calif.
- Sinton, J. B., and D. M. Hussong (1983), Crustal structure of a short length transform fault in the central Mariana Trough, in *The Tectonic and Geologic Evolution of Southeast Asian Seas and Islands: Part 2*, edited by D. E. Hayes, pp. 236–254, AGU, Washington, D. C., doi:10.1029/GM027p0236.
- Stern, R. J. (2002), Subduction zones, *Rev. Geophys.*, *40*(4), 1012, doi:10.1029/2001RG000108.
- Stern, R. J. (2010), The anatomy and ontogeny of modern intra-oceanic arc systems, in *The Evolving Continents: Understanding Processes of Continental Growth*, edited by T. M. Kusky, M.-G. Zhai, and W. Xiao, Geol. Soc. Spec. Publ., *338*, 7–34.
- Stern, R. J., N. C. Smoot, and M. Rubin (1984), Unzipping of the volcano arc, Japan, *Tectonophysics*, *102*, 153–174, doi:10.1016/0040-1951(84)90012-X.
- Stern, R. J., S. H. Bloomer, F. Martinez, T. Yamazaki, and T. M. Harrison (1996), The composition of back-arc basin lower crust and upper mantle in the Mariana Trough: A first Report, *Isl. Arc*, *5*, 354–372, doi:10.1111/j.1440-1738.1996.tb00036.x.
- Stern, R. J., M. J. Fouch, and S. L. Klemperer (2003), An overview of the Izu-Bonin-Mariana subduction factory, *Geophys. Monogr.* *138*, 175–222.
- Stern, R. J., E. Kohut, S. H. Bloomer, M. Leybourne, M. Fouch, and J. Vervoort (2006), Subduction factory processes beneath the Guguan cross-chain, Mariana Arc: No role for sediments, are serpentinites important?, *Contrib. Mineral. Petrol.*, *151*, 202–221, doi:10.1007/s00410-005-0055-2.
- Stern, R. J., Y. Tamura, H. Masuda, P. Fryer, F. Martinez, O. Ishizuka, and S. H. Bloomer (2013), How the Mariana Volcanic Arc ends in the south, *Isl. Arc*, *22*, 133–148, doi:10.1111/iar.12008.
- Stern, R. J., et al. (2014), Volcanoes of the Diamante cross-chain: Evidence for a mid-crustal felsic magma body beneath the Southern Izu-Bonin-Mariana arc, in *Orogenic Andesites and Crustal Growth*, edited by A. Gomez-Tuena, S. M. Straub, and G. F. Zellmer, Geol. Soc. Spec. Publ., *385*, 235–255.
- Stüben, D., T. Neumann, N. E. Taibi, and G. P. Glasby (1998), Segmentation of the southern Mariana back-arc spreading center, *Isl. Arc*, *7*, 513–524, doi:10.1111/j.1440-1738.1998.00207.x.
- Taylor, B. (1992), Rifting and the volcanic-tectonic evolution of the Izu-Bonin-Mariana arc, in *Proceedings of the Ocean Drilling Program, Scientific Results*, vol. 126, edited by B. Taylor et al., pp. 627–651, Ocean Drill. Program, College Station, Tex.
- Taylor, B. (Ed.) (1995), *Backarc Basins: Tectonics and Magmatism*, Springer, New York, doi:10.1007/978-1-4615-1843-3.
- Taylor, B., K. Crook, and J. Sinton (1994), Extensional transform zones and oblique spreading centers, *J. Geophys. Res.*, *99*(B10), 19,707–19,718, doi:10.1029/94JB01662.
- Taylor, B., A. M. Goodliffe, G. F. Moorel, A. J. Oakley, P. Fryer, and EW0202 Scientific Party (2002), Multi-channel seismic images of the Mariana Trough: EW0202 initial results, *EOS Trans. AGU*, *83*(47), Fall Meet. Suppl., Abstract, T72A-1228.
- Thouret, J.-C. (1999), Volcanic geomorphology: An overview, *Earth Sci. Rev.*, *47*, 95–131, doi:10.1016/S0012-8252(99)00014-8.
- Tucholke, B. E., J. Lin, and M. C. Kleinrock (1998), Megamullions and mullion structure defining oceanic metamorphic core complexes on the Mid-Atlantic Ridge, *J. Geophys. Res.*, *103*(B5), 9857–9866, doi:10.1029/98JB00167.
- Urabe, T., J. Ishibashi, A. Maruyama, K. Marumo, N. Seama, and M. Utsumi (2004), Discovery and drilling of on- and off-axis hydrothermal sites in backarc spreading center of southern Mariana Trough, western Pacific, *EOS Trans. AGU*, *85*(47), Fall Meet. Suppl., Abstract, V44A-03.
- Uyeda, S., and Z. Ben-Avraham (1972), Origin and development of the Philippine Sea, *Nature*, *238*, 176–178.
- Vallier, T., et al. (1991), Subalkaline andesite from Valu Fa Ridge, a back-arc spreading center in southern Lau Basin: Petrogenesis, comparative chemistry, and tectonic implications, *Chem. Geol.*, *91*, 227–256, doi:10.1016/0009-2541(91)90002-9.
- van der Hilst, R., and T. Seno (1993), Effects of relative plate motion on the deep structure and penetration depth of slabs below the Izu-Bonin and Mariana island arcs, *Earth Planet. Sci. Lett.*, *120*, 395–407, doi:10.1016/0012-821X(93)90253-6.
- Vogt, P. R. (1973), Subduction and aseismic ridges, *Nature*, *242*, 189–191, doi:10.1038/242117a0.
- Vogt, P. R., A. Lowrie, D. R. Bracey, and R. N. Hey (1976), Subduction of aseismic oceanic ridges: Effects on shape, seismicity, and other characteristics of consuming plate boundaries, *Spec. Pap. Geol. Soc. Am.*, *172*, 1–59, doi:10.1130/SPE172-p1.

- Walker, G. P. L. (1993), Basaltic-volcano systems, in *Magmatic Processes and Plate Tectonics*, vol. 76, edited by H. M. Prichard et al., *Geol. Soc. Spec. Publ.*, 76, 3–38.
- Wallace, L., R. McCaffrey, J. Beavan, and S. Ellis (2005), Rapid microplate rotations and backarc rifting at the transition between collision and subduction, *Geology*, 33(11), 857–860, doi:10.1130/G21834.1.
- Wessel, P., K. J. Matthews, R. D. Müller, A. Mazzoini, J. M. Whittaker, R. Myhill, and M. T. Chandler (2015), Semiautomatic fracture zone tracking, *Geochem. Geophys. Geosyst.*, 16, 2462–2472, doi:10.1002/2015GC005853.
- Wheat, C. G., P. Fryer, S. Hulme, N. Becker, A. Curtis, and C. Moyer (2003), Hydrothermal venting in the southernmost portion of the Mariana backarc spreading center at 12°57'N. *EOS Trans. AGU*, 84(46), Fall Meet. Suppl., Abstract, V32A-0920.
- Widiyantoro, S., B. L. N. Kennett, and R. D. van der Hilst (1999), Seismic tomography with P and S data reveals lateral variations in the rigidity of deep slabs, *Earth Planet. Sci. Lett.*, 173(1–2), 91–100, doi:10.1016/S0012-821X(99)00216-2.
- Wilcock, W. S. D. (1998), Cellular convection models of mid-ocean ridge hydrothermal circulation and the temperatures of black smoker fluids, *J. Geophys. Res.*, 103(B2), 2585–2596, doi:10.1029/97JB03252.
- Yamazaki, T., F. Murakami, and E. Saito (1993), Mode of seafloor spreading in the northern Mariana Trough, *Tectonophysics*, 221(2), 207–222, doi:10.1016/0040-1951(93)90333-F.
- Yeo, I., R. C. Searle, K. L. Achenbach, T. P. Le Bas, and B. J. Murton (2012), Eruptive hummocks: Building blocks of the upper ocean crust, *Geology*, 40(1), 91–94, doi:10.1130/G31892.1.
- Yeo, I. A., C. W. Devey, T. P. LeBas, N. Augustin, and A. Steinführer (2016), Segment-scale volcanic episodicity: Evidence from the North Kolbeinsey Ridge, Atlantic, *Earth Planet. Sci. Lett.*, 439, 81–87, doi:10.1016/j.epsl.2016.01.029.
- Yoshikawa, S., K. Okino, and M. Asada (2012), Geomorphological variations at hydrothermal sites in the southern Mariana Trough: Relationship between hydrothermal activity and topographic characteristics, *Mar. Geol.*, 303–306, 172–182, doi:10.1016/j.margeo.2012.02.013.
- Zhang, Y., S. Z. Li, Y. H. Suo, L. L. Guo, S. Yu, I. D. Somerville, R. H. Guo, Y. B. Zang, Q. L. Zheng, and D. L. Mu (2016), Origin of transform faults in back-arc basins: Examples from Western Pacific marginal seas, *Geol. J.*, 51(S1), 490–512, doi:10.1002/gj.2807.